8-2004

A Site-Specific Indoor Wireless Propagation Model

Chen Jin
University of Tennessee - Knoxville

To the Graduate Council:

I am submitting herewith a thesis written by Chen Jin entitled "A Site-Specific Indoor Wireless Propagation Model." I have examined the final electronic copy of this thesis for form and content and recommend that it be accepted in partial fulfillment of the requirements for the degree of Master of Science, with a major in Electrical Engineering.

Mostofa K. Howlader, Major Professor

We have read this thesis and recommend its acceptance:

Gregory Peterson, Aly Fathy, Stephen F. Smith

Accepted for the Council:
Carolyn R. Hodges

Vice Provost and Dean of the Graduate School

(Original signatures are on file with official student records.)

To the Graduate Council:

I am submitting herewith a thesis written by Chen Jin entitled “A Site-Specific Indoor Wireless Propagation Model.” I have examined the final electronic copy of this thesis for form and content and recommend that it be accepted in partial fulfillment of the requirements for the degree of Master of Science, with a major in Electrical Engineering.

Mostofa K. Howlader
Major Professor

We have read this thesis
and recommend its acceptance:

Gregory Peterson

Aly Fathy

Stephen F. Smith

Accepted for the Council:

Anne Mayhew

Vice Chancellor and
Dean of Graduate Studies

(Original signatures are on file with official student records.)

A Site-Specific Indoor

Wireless Propagation Model

A Thesis Presented for the

Master of Science

The University of Tennessee, Knoxville

Chen Jin

August 2004

Acknowledgements

I would like to thank my M.S. advisor and Committee Chairman Dr. Howlader first, for always having his office door open, pointing me in the right direction on a number of issues and giving me lots of books to read. I benefited greatly from his insightful comments, discussions and revisions, which have made this document more readable and accurate. I would also like to express my appreciation to Dr. Smith, Dr. Peterson, and Dr. Fathy for serving as my Committee members, and their time and patience in reading this thesis. In addition, I would like to give my special thanks to Dr. Smith for his insight and plentiful help in solving the difficulties encountered in the research, as well as providing valuable feedback and suggestions to improve my thesis content and presentation.

This research work has been performed in the Wireless Communications Research Group (WCRG) at University of Tennessee, Knoxville, with support from the RF & Microwave System Group (RFMSG) of the Oak Ridge National Laboratory (ORNL), and sponsored by the United State Nuclear Regulatory Commission (NRC). With their generous financial support, I have been able to pursue my chosen program of study here. I gratefully acknowledge the staff and personnel in the RF & Microwave System Group and the students in the WCRG. Without their invaluable assistance, I would not have been able to accomplish this degree. I am also especially indebted to Paul Ewing, leader of the RFMSG, who has provided me with this great opportunity. The last line is always reserved for my parents, who helped me through this arduous thesis writing process with their encouragement and mental support.

Chen Jin

Knoxville, 2004

Abstract

In this thesis, we explore the fundamental concepts behind the emerging field of site-specific propagation modeling for wireless communication systems. The first three chapters of background material discuss, respectively, the motivation for this study, the context of the study, and signal behavior and modeling in the predominant wireless propagation environments. A brief survey of existing ray-tracing based site-specific propagation models follows this discussion, leading naturally to the work of new model development undertaken in our thesis project. Following the detailed description of our generalized wireless channel modeling, various interference cases incorporating with this model are thoroughly discussed and results presented at the end of this thesis.

Table of Contents

List of Tables

List of Figures

Chapter 1

Introduction

Recent years have brought the indoor and individual wireless communication markets unprecedented opportunities as well as new challenges for achieving higher quality, speed, coverage, and reliability. To meet such market demands, progressively more researchers have focused on performance simulations of the various wireless standards, in which the use of an accurate yet efficient propagation model is essential for credible performance prediction in practical situations. Presently, there exist numerous statistically based channel models, which are generally considered adequate for outdoor environments or macro-cell system planning. For indoor wireless services, though, these statistically based models do not provide sufficient site-specific information because of the complexities and variations of the propagation environments, which are usually rich in reflections and scattering. Although the signal propagation characteristics can be accurately obtained by explicitly solving the Maxwell's equations with the surrounding geometry as boundary conditions, the process is unreasonably cumbersome and impractical if not actually intractable for more complex environments. Databases based on site-specific measurements are usually not very practical either.

A more generalized, computationally feasible site-specific propagation model, based on geometrical ray tracing, can be used to predict details about a specific site with known parameters such as geometry and building materials. Usually the model needs to be parameterized and adjustable in terms of the received power threshold, path number, delay array and power array and so on, depending on the author's mathematical channel expression. Accordingly, a suitable model for most any indoor situation can be generated by adjusting these specific parameters. Moreover, the model needs to be sufficiently general to accommodate signal properties such as polarization, correlation, coupling loss, and channel parameters such as geometry, Doppler shifts, dielectric constants, and the like.

In this research, we propose a new generalized, semi-deterministic, polarization-sensitive multipath channel model to more accurately predict the propagation of various types of wireless signals in urban environments, especially inside and around industrial plant structures, warehouses, buildings, and the like. The front-end electromagnetic field calculations needed to analyze the propagation environment are performed by the Wireless InSite program from Remcom, Inc. [1]. The InSite analysis provides the total delays, delay spreads, and individual path losses, phases, and reflection coefficients for all principal paths based on a selectable receiver-signal threshold. We have provided an example for showing the system performance using our technique, where InSite calculates the necessary parameters for the propagation in a specified signal environment, and a MATLAB/Simulink model evaluates the link performance for different wireless local-area network (WLAN) system for both pure AWGN and multipath cases.

As digital WLANs become increasingly prevalent, the physical layer performance is critical for the successful implementation and application of the whole system. From a communications engineering perspective, the challenge is to build up an accurate system model, including transmitter and receiver devices, as well as the propagation channel model, and to fully represent the various specifications, power level, bit rate, signal-noise-ratio, receiver sensitivity, and so forth. We will therefore focus our research on these two issues: first, to develop a more accurate and applicable wireless propagation model for our desired environments, including industrial plants, warehouses, and the like; and second, to simulate the coexistence interference among the several most used wireless protocols, which share the same spectrum at 2.45 GHz: Wi-Fi, Bluetooth and Zigbee. Aiming at these two goals, a brief introduction about the RF specifications of these protocols is given in Chapter 2, along with a description of the coexistence scenarios or cases which will be covered later in the study.

In Chapter 3, a brief overview of the prevalent the propagation modeling techniques is presented. Although there are numerous statistically based propagation modeling methods in the literature, we will focus on the ray-tracing based method, since the prime requirement for the model application is accuracy, and the site-specific information needs

to be incorporated into the overall propagation model. Historically, work on ray-tracing techniques has been proposed for the computer vision field based on ray-optics theory. Similarly to light, the behavior of the high-frequency electromagnetic waves can be considered as rays or ray-beams; a ray-tracing based methodology was first adopted in the wireless field by McKown and Hamilton [2]. A more detailed survey of more recent ray-tracing based propagation models can be found in Chapter 3.

In Chapter 4, our new semi-deterministic site-specific propagation model is presented in detail, including site-specific effects and signal attributes such as polarization.

In Chapter 5, we present the computational results on the various protocols, with white noise, general fading effects, room-specific propagation models, and cross-protocol interference effects, both with and without fading. The results focus on WiFi and Bluetooth systems but are generalized to other types of signals. In addition, some implementation issues encountered in the system simulations are discussed.

Finally, in chapter 6, we provide a summary of the research and some conclusions. In general, the utility of site-specific propagation is demonstrated. We also provide possible directions for future work in this research area.

Chapter 2

Wireless Protocols and Interference Models

In this chapter, the introduction of several common protocols used in the wireless local area networks (WLANs) is briefly discussed in terms of power levels, transmission and receiver schemes, bit rates, and operating bandwidth. Following is a description of coexistence and interference scenarios for the various wireless devices.

2.1 Wireless Links

In making decisions on the deployment of wireless systems, it is not enough to choose a technology to meet a particular application. Thus, several types of wireless devices need to be involved in our simulation experiments for the general industrial and nuclear power-plant (NPP) environment. First, mobile phones and Personal Communication System (PCS) devices are considered since they have already been used in industrial settings and NPPs as long-range communication technologies. Then, the models of transmitters and receivers for several promising wireless communication technologies used in short-range applications are presented, namely, Bluetooth, 802.11b, UWB and ZigBee. These technologies are gaining increasingly interest from industry.

2.1.1 Cell-phone / PCS models

Most cell phones actually operate in three modes, including both analog and digital in the 800 MHz band and can also accommodate the PCS band at 1.8 GHz. The analog format has the widest coverage of any system, with service available in almost any city or town, and on most major highways in the U. S. For this reason, analog cellular in the 800-MHz band will remain the dominant wireless communication options in rural areas for some time to come, although digital CDMA services are being added quickly in most parts of the U. S. In addition, most cell phones nowadays operate primarily in the PCS band, particularly in the areas of higher population density.

PCS is a new class of communications technology that not only permits high-quality digital voice wireless communications but also provides high-rate data services, such as internet connections. All PCS systems use digital technology for transmission and reception. There are two types of PCS services: narrowband and broadband. The frequency bands used by PCS devices are outlined in Table 2.1.

2.1.2 Two-way Radios

Two-way radios are typically used in the industrial and NPP environments by plant operations, maintenance, and security personnel for general voice communications. These units invariably operate in bands in very-high frequency (VHF) and/or ultra-high frequency (UHF) regions of the spectrum. Power levels can vary from about 100 mW to several watts, depending on the range required.

Table 2.1 PCS frequency allocations.

Type	Lower (MHz)	Upper (MHz)
Narrowband	900	901
Narrowband	930	931
Narrowband	940	941
Broadband	1850	1910
Unlicensed	1910	1930
Broadband	1930	1990

2.1.3 Bluetooth

Bluetooth is a method for data and voice communication that uses short-range (<10m) radio links to replace cables between personal computers, handhelds, mobile phones, and other electronic devices, as well as access to networked resources. Bluetooth employs a simple frequency hopping scheme with 79 channels in the 83.5 MHz-wide Industrial, Scientific, and Medical (ISM) band at 2.45 GHz. It uses Gaussian-filtered frequency-shift keying (GFSK) modulation. The primary use of Bluetooth in the NPP environments will be typically for interconnection of digital devices, such as personal digital assistants (PDAs), Palm computers, and possibly wireless sensors. These devices generally operate with power levels from 1 to 100 mW, although usually at the lower end of the power range.

2.1.4 The IEEE 802.11 Family of Standard Protocols

2.1.4.1 IEEE 802.11a

802.11a is another IEEE standard WLAN protocol which utilizes an Orthogonal frequency-division multiplex (OFDM) scheme to achieve data rates as high as 54 Mbps in the 5.8-GHz ISM band. The anticipated application of 802.11a in NPPs will be for high-rate point-to-point data links and in general computer wireless networking. An obvious advantage of 802.11a is that it operates in a different frequency band from the other 802.11 devices and thus would be much less likely to receive or generate interference with respect to those devices.

2.1.4.2 IEEE 802.11b

802.11b (Wi-Fi) is the popular term for a high-frequency wireless local-area network (WLAN) as a specification from the IEEE and a part of a family of wireless specifications together with 802.11, 802.11a, and 802.11g, and others. The 802.11b (Wi-Fi) technology operates in the 2.4-GHz range, offering data speeds up to 11 Mbps. The modulation used in 802.11 has historically been phase-shift keying (PSK). The

modulation method selected for 802.11b is known as complementary-code keying (CCK), which allows higher data speeds and is somewhat less susceptible to multipath-propagation interference. The 802.11b signal is spread-spectrum modulated by a standard, fixed 11-bit Barker code and offers modest resistance (about 10 dB) to interference and multipath effects.

2.1.4.3 IEEE 802.11g

802.11g, another IEEE standard for WLANs, offers wireless transmission over relatively short distances at up to 54 Mbps compared with the maximum 11 megabits per second of the 802.11b (Wi-Fi) standard. Like 802.11b, 802.11g operates in the 2.4-GHz range, while its data rate can be compatible with 802.11a (HiperLAN2). The 802.11g utilizes a complex OFDM scheme to achieve higher data rates and afford greater resistance to multipath effects than earlier schemes.

2.1.5 Ultra-wideband (UWB) (IEEE 802.15.3)

UWB, as defined by Federal Communications Commission (FCC), is a technology having a spectrum that occupies a bandwidth greater than 25% of the center frequency or at least 500 MHz. As a promising technology for high-rate, short-range communications, it has potential cost and power consumption advantages over comparable narrowband technologies at short range; furthermore, it opens up 7.5 GHz of new spectrum to allow for more unlicensed devices to share the same space as current licensed [cellular, FWA, global positioning system (GPS)] and unlicensed systems [WLANs, wireless personal-area network (WPANs)]. Besides, there are other benefits from UWB due to its wideband nature, e.g., great channel capacity, fading robustness, accurate position location, and so forth. The current efforts at standardizing UWB transmissions are focusing on the range from 3 to 5 GHz. The two basic formats in most favor are a binary phase-shift keying (BPSK)-modulated signal proposed by Xtreme Spectrum, Inc. of Vienna, VA and an OFDM format promoted by Intel and Texas Instruments. As of this writing, no clear winner has emerged and few commercial UWB products are yet available.

2.1.6 ZigBee (IEEE 802.15.4)

ZigBee, invented by Philips Semiconductors, is a simpler, slower, lower-power, lower-cost cousin of Bluetooth. The standard originates from the Firefly Working Group and is finding widespread acceptance within the industry with a specification providing for up to 254 nodes including one master, managed from a single remote control. Turning lights on, setting the home security system, starting the video cassette player (VCR) - all these can be done from anywhere in the home at the touch of a button. Besides home automation, low data rate wireless connectivity supports voice and data transfer, and personal computer (PC) to input device (keyboard, mouse) communications.

2.1.7 General-Purpose ISM devices

The FCC has designated three license-free bandwidth segments ISM use in the United States. They are the:

- 902 to 928 MHz ISM band;
- 2.450 to 2.4835 GHz ISM band;
- 5.1 to 5.85 GHz band (U–NII / ISM bands).

All countries have adopted at least a part of the 2.45 GHz band, making it the de facto worldwide standard for license-free ISM communications. There are also numerous devices with non-standard, proprietary protocols which nevertheless produce high quality transmission.

While promising a variety of applications, the wireless technologies listed in Table 2.2 face substantial questions about their real-world effectiveness, about the interference effects on other spectrum users, and about whether nuclear-plant regulators will permit their widespread use. Thus, a detailed investigation of these wireless links in the varied environments of the typical NPP is essential for effective deployment of wireless systems,

Table 2.2 Comparison of various RF wireless links.

Wireless technologies	Freq. Band (GHz)	Bit rate (Mb/s)	Range (m)	Multiple Access Method	Modulation
Bluetooth1.1	2.4-2.4835	1	10	FHSS	GFSK
Wi-Fi (802.11b)	2.4-2.4835	~ 11	100	DSSS	CCK QPSK
802.11g	2.4-2.4835	~ 54	100	OFDM	CCK
ZigBee (802.15.4)	2.4-2.4835 0.902-0.928	0.250	10	DSSS	O-QPSK BPSK
Cell phone (IS-95)	RX: 0.869-0.894 TX: 0.824-0.849	1.2288	Long-distance	TDMA FDM	QPSK OQPSK
PCS phone (High Tier, US)	TX: 1.85-1.91 RX: 1.93-1.99	0.384	Long-distance	π/4-DQPSK	TDMA FDMA
UWB (802.15.3)	3.1-5.1	110	10	TH/PPM DSSS OFDM	Bi-phase QPSK

both from the standpoint of accurate data communications and the avoidance of RF interference.

2.2 Interference Models

2.2.1 Propagation-based Interference Study

For the purpose of analyzing the coexistence issue, a proximally located layout of different devices must be postulated. For instance, in order to analyze the reliability of a Bluetooth (BT) piconet in the presence of interference from other types of radio links, it is assumed that there is one BT piconet co-located with an 802.11b PDA. The BT piconet consists of two BT devices, which are capable of establishing at least a point-to-point link. These devices are limited to 0 dBm transmit power. To make the scenario realistic, more devices such as UWB, cell phone, 802.11g router, and so forth can be added as interferers on a step-by-step basis. In the same fashion, the effects of interference upon receivers in 802.11b/g, UWB or ZigBee systems can be investigated. Fig. 2.1 below is one typical operational scenario presenting all kinds of interferers within the proximity of a Bluetooth RX in an industrial environment. Personal networking and communication devices, such as ZigBee connected keyboards, cell phones and two-way radios may be operated in close proximity to the target receiver, whereas other types of plant systems need to be operated at significantly greater distances.

2.2.2 Diagram of Overall Analysis

Since the propagation channel has different statistical characteristics with different pairs of transmitters and receivers, it is necessary to come up with a general channel model suitable for both narrowband and wideband systems. This model will be detailed in the next section. The full-fledged test model for Bluetooth receiver is visualized in Fig. 2.2. As shown in the model, the received signal for the Bluetooth Rx is a superposition of all the transmitted signals. It is to be noted that the Bluetooth receiver box can be replaced with an 802.11b, ZigBee, UWB, cell phone or PCS RX as desired in the simulations.

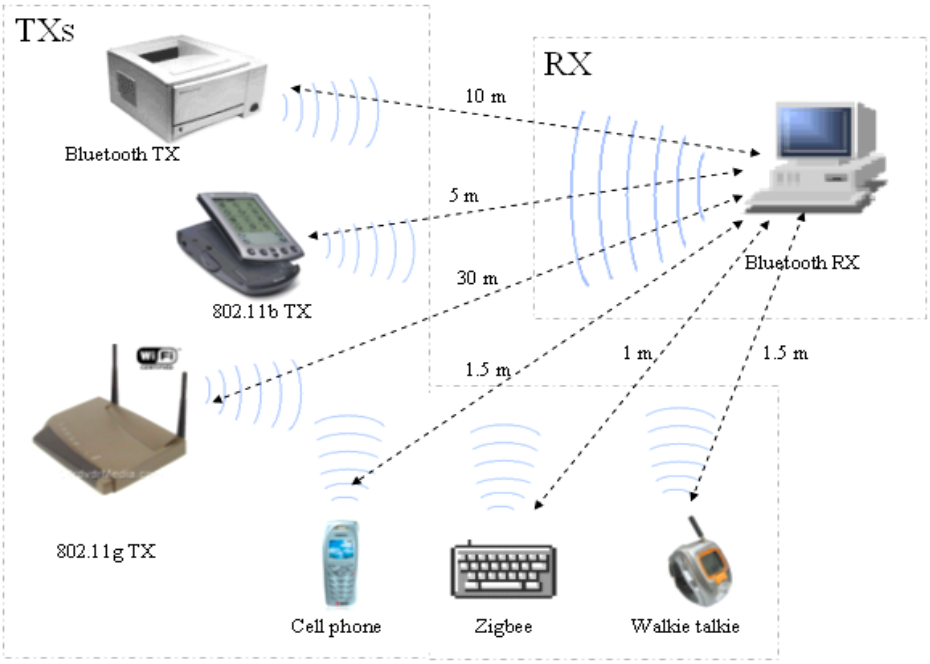

Fig. 2.1 One possible layout of measurement set.

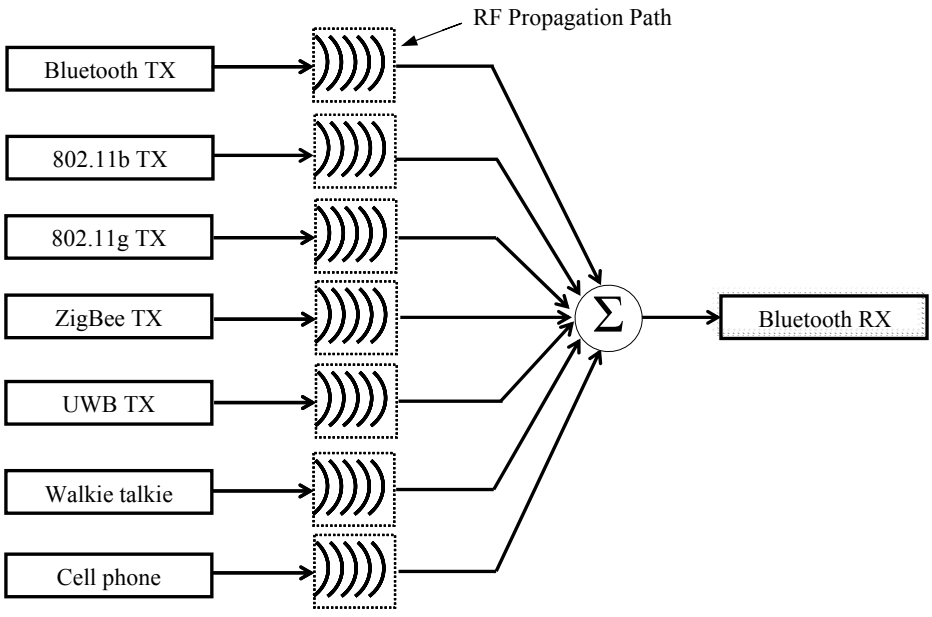

Fig. 2.2 Comprehensive test model for interference on Bluetooth RX.

Chapter 3

The Radio Propagation Channel

We are living with an ever-increasing demand on telecommunications speed and ubiquity; the advent of the Internet and data networks has only served to escalate this trend. Their mobility and ease of installation make wireless communication networks one of the most important communication systems to deploy. Personal communication systems (PCS), wireless local area networks (WLANs), cellular telephones, paging services, and the wireless sensing devices are being deployed in indoor areas on an increasing scale, even reaching into offices, shopping malls, schools, hospitals, and factories. Because indoor radio channels often have a significant amount of impairments and variability, large-scale deployment of these services provides a major challenge to wireless network designers. For this reason, it is imperative to develop deployment tools, which provide both efficient and accurate radio channel models. The efficiency of a model is generally measured by its computational complexity, whereas the accuracy of the model is measured by the overall performance estimation error. Although most of the current research in modeling and simulation of the wireless channel has been done for mobile radio and residential and office environments, the propagation modeling for industrial and other adverse areas has not been fully investigated. Therefore we will focus our discussions on the propagation model for wireless communications in urban and industrial environments, chiefly in multipath-prone indoor applications.

In what follows, we will present the general aspects of the wireless propagation characteristic. Then a variety of modeling methods will be covered. Finally, research work using ray-tracing and related propagation models will be fully discussed.

3.1 Introduction to the Radio Propagation Channel

As mentioned above, the successful implementation of a wireless network requires an exact understanding of the radio propagation characteristics. Therefore, the physical

mechanisms presented in general wireless channels, mainly comprised of multipath effects and fading will be described, as well as polarization properties inherent in the channel to handle the effects of antennas and wave interactions in the propagation models.

3.1.1 Multipath

A portion of the waves emitted from a transmitter arrive directly at a receiver if there is a line-of-sight (LOS) path, usually with the strongest power and shortest delay of all the received-signal components. In practice, wireless channels are not very friendly and usually have a variety of scatterers between the transmitter and receiver, which results in another portion of propagated waves reaching the receiver after experiencing several interactions such as reflections, refractions, diffractions, and scattering. Multipath results from the fact that the propagation channel consists of several obstructions and reflectors. Thus the received signal arrives as a seemingly largely unpredictable set of reflected and direct waves, each with its own degree of attenuation and delay. These signal components can constructively or destructively add to give a received signal that varies significantly in both amplitude and phase.

The scattering effect for each path can be modeled as multiple components, represented as random phase shifts and amplitude fluctuations of this dominant component. The lowpass-equivalent impulse response of a discrete multipath channel is given by

$$\tilde{c}(t,\tau_k,\phi_k) = \sum_{k=0}^{\infty} \tilde{c}_k(t,\tau_k,\phi_k)\cdot\delta(t-\tau_k), \tag{3.1}$$

where the resultant complex polar signal components are given by

$$\tilde{c}_k(t,\tau_k,\phi_k) = \left|\tilde{c}_k(t,\tau_k,\phi_k)\right| e^{j\theta_k}, \tag{3.2}$$

where $\tilde{c}_k(t,\tau_k,\phi_k)$ is a complex random process in t, τ_k is the relative time delay of the kth multipath component (k = 0 to ∞), ϕ_k is the angle-of-arrival of the kth multipath

component, and $\delta(\cdot)$ is the unit impulse function. In Eq. (3.2), θ_k represents the received phase for the *k*th path.

For simplicity, an omnidirectional antenna is assumed to be used in the receiver so that the effect of ϕ_k can usually be ignored. For many channels, a reasonable approximation is often made that the number of discrete components is limited and constant and that the path delay values vary slowly and can also be assumed approximately constant. The model then simplifies to

$$\tilde{c}(t,\tau_k) = \sum_{k=0}^{L} \tilde{c}_k(t) \cdot \delta(t-\tau_k), \tag{3.3}$$

where (L+1) is the total possible number of multipath components. Similar to [3], an example of different snapshots of $|\tilde{c}(t,\tau_k)|$ is illustrated Fig. 3.1, where *t* points out the page.

3.1.2 Fading

Because of the multipath phenomenon above, the total received signals are the superposition of all the rays from different paths, each with a different amplitude and phase. These paths can be summed constructively or destructively, and thereby lead to an

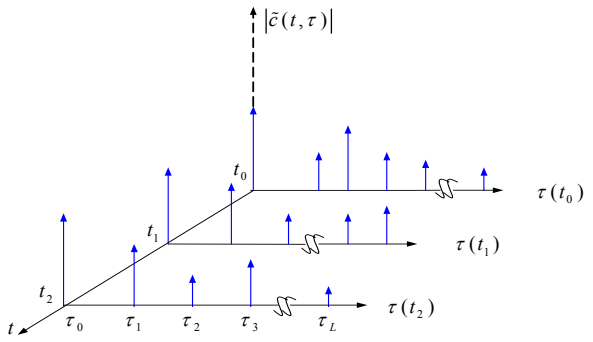

Fig. 3.1 A time-varying discrete-time impulse response for a multipath radio channel [3].

amplitude which fluctuates rapidly with time and small movements, which in turn have a direct effect on the received signals' phases.

3.1.3 Polarization Issues

Like frequency and wavelength, polarization is a fundamental property of an electromagnetic wave. Also, it is a very important aspect in light of both wave propagation mechanisms and antenna patterns. A polarized wave can be represented mathematically as the vector sum of vertical and horizontal components. Based on the phenomenon that the polarization will be rotated after reflections, the reflection coefficient is divided into these two directions accordingly, which is given by [4]

$$\begin{cases} \Gamma_{\perp} = \dfrac{-\varepsilon_r \sin\theta_i + \sqrt{\varepsilon_r - \cos^2\theta_i}}{\varepsilon_r \sin\theta_i + \sqrt{\varepsilon_r - \cos^2\theta_i}} \\ \Gamma_{//} = \dfrac{\varepsilon_r \sin\theta_i - \sqrt{\varepsilon_r - \cos^2\theta_i}}{\varepsilon_r \sin\theta_i + \sqrt{\varepsilon_r - \cos^2\theta_i}} \end{cases}, \tag{3.4}$$

where ε_r is the relative value of permittivity, and θ_i is the incident angle. Also, the propagating wave will be influenced differently for different polarization through the medium.

3.2 Types of Channel Modeling

We now present most relevant and important research effort and results on radio channel modeling which have been done so far. In general, the existing channel modeling methodologies are divided into the three main categories: empirical, statistical, and deterministic. In this chapter, based on their conclusions, we will mostly concentrate on ray-tracing methods and the like, along with briefly introducing other channel models.

Empirical modeling is a method which requires a significant amount of human resources and expensive equipment to do the field measurements. It is usually implemented by the channel-sounding techniques for wideband and narrowband signals respectively.

Compared with the other two methods, empirical modeling does not have as great an application value; however, it can be considered as a benchmark to verify the accuracy of statistical and deterministic modeling.

In order to save time and human resources for field measurement and provide quicker deployment of wireless networks**,** much attention has been paid to developing software-based computational channel simulators, which facilitate a deeper understanding of the impact of propagation in the wireless channel without the need for exhaustive RF measurements. Since the mid 1970s, numerous wireless channel models have been presented for both outdoor and indoor wireless environments. Most of them can be divided into two main categories: statistical and deterministic. The statistical models are easily expressed in terms of parameters that can be used in the simulation of wireless communications systems, such as approximate delay spread, direction of arrival, and bit error rates. In a word, statistical models provide parameters suitable for system simulations but lack great specificity and accuracy. Electromagnetic (EM)-based deterministic models, on the other hand, can provide highly accurate and site-specific coverage and delay spread information but also can be very computationally inefficient and time consuming.

3.2.1 Statistical Channel Modeling

Statistical methods are usually divided into three aspects: path loss, large-scale fading, and small-scale fading, each of which is caused by different propagation mechanisms.

3.2.1.1 Path Loss and Large-Scale Fading

The most widely used statistically based methods of representing RF propagation path loss within statistical propagation models are the class of slope-intercept models, also called *log-distance* models. These models treat the propagation loss as being comprised of a distance-related deterministic component as well as statistical components both for the shadowing and/or scattering effects on the received-signal amplitudes or powers. The deterministic component is taken to be of the form

$$L_p(\mathrm{d}) = L_p(\mathrm{d}_0) + 10\ m\ \log(\mathrm{d}/\ \mathrm{d}_0) + \mathrm{X}_\sigma, \quad \textbf{(3.5)}$$

where d is the distance in meters, L_p the path loss in decibels, and m the path loss index; d_0 is the reference distance. The shadowing effect is represented by X_σ in decibels, which follows approximately a Gaussian distribution, with standard deviations depending on the specific local signal-propagation environment.

The path-loss expression above reveals how the received power depends on receiver location for a fixed transmitter. The total received power depends on the distance between transmitter and receiver, plus the effects of fading and reflections. Due to radio wave reflections from metal walls, tanks, machinery, and the like in typical indoor industrial environments, m is usually less than 2 (2 stands for the free-space case), which means the received power attenuation due to the transmitter/receiver separation will be less than in corresponding outdoor environments.

Some measurements [5] in factories show the value of m ranges from 1.1 to 1.8. For the sake of simplicity, the standard free-space path loss model is adopted in our simulations, obviously but it can be easily modified to the actual m.

3.2.1.2 Small-Scale Fading

By virtue of the central limit theorem, the channel response $\tilde{c}_k(t, \tau_k, \phi_k)$ can be modeled as a complex Gaussian process, since the components of the multipath signal arise from a large number of individual reflections and isotropic scattering. At any time t, the probability density functions of the real and imaginary parts are Gaussian. This model implies that for each τ_k the ray is composed of a large number of irresolvable components. If $\tilde{c}_k(t, \tau_k, \phi_k)$ has a zero mean, then the envelope $R_k(t, \tau_k, \phi_k) = \left|\tilde{c}_k(t, \tau_k, \phi_k)\right|$ has a Rayleigh probability density function

$$f_R(r) = \frac{r}{\sigma^2} e^{-r^2/(2\sigma^2)}, \quad \textbf{(3.6)}$$

θ_k, therefore, has a uniform distributed over the interval 0 to 2π.

If there is a dominant component present, the attenuation will be considered as a Rician distribution, but the phase will no longer have a uniform distribution due to the presence of the finite direct component. The Rician probability density function is

$$f_R(r) = \frac{r}{\sigma^2} I_0\left[\frac{Ar}{\sigma^2}\right] e^{-(r^2+A^2)/(2\sigma^2)}, \quad \textbf{(3.7)}$$

where A is the nonzero mean of $\tilde{c}_k(t, \tau_k, \phi_k)$ and $I_0[\cdot]$ is the zeroth-order modified Bessel function of the first kind.

The ratio K=$\frac{A^2}{\sigma^2}$, usually referred to as the Rician factor, is an indicator of the relative power in the specular and scattered components. For values of K >> 1 the channel tends to be essentially specular and its pdf is approximately Gaussian about the mean, whereas for K << 1 the channel tends to be Rayleigh, which is verified by Fig. 3.2. In the simulation model, the specular and the Rayleigh components are implemented separately.

While the pdf of $|\tilde{c}_k(t, \tau_k, \phi_k)|$ describes the distribution of the instantaneous values of the impulse response, the temporal variations are modeled by an appropriate autocorrelation function or, equivalently, by the power spectral density of the random process as a function of *t*.

3.2.1.2.1 Time correlation - Doppler Effect

Coherence time represents the time separation over which the channel impulse responses at two time instants remain strongly correlated. The coherence time is inversely proportional to the Doppler spread and is a measure of how fast the channel changes in time -- the larger the coherence time, the slower the channel changes.

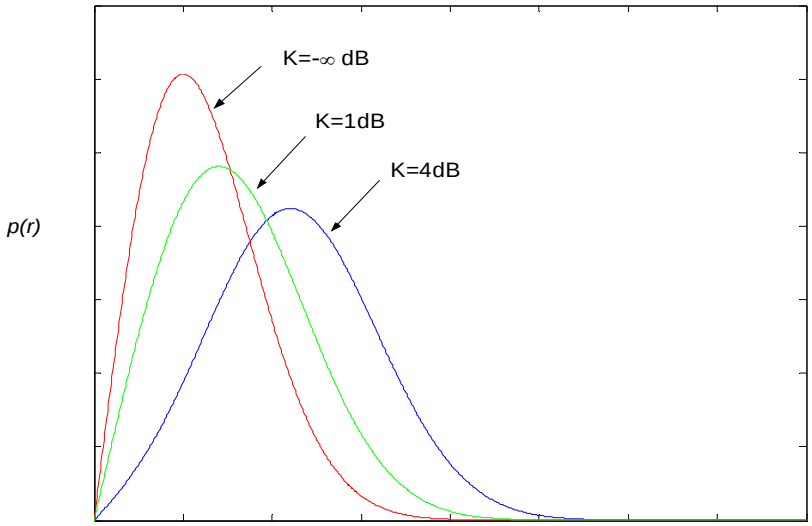

Fig. 3.2 Rician probability density function (pdf).

Despite the much lower speed of relative TX/RX mobile velocities within most urban areas, as well as industrial plants and buildings, the usual form of analysis of the Doppler spectrum still uses the classical Jakes power spectrum density (PSD) [6], which was initially developed for the outdoor mobile (cell-phone) case. For the indoor industrial case, the fading rate (the product of the maximum Doppler frequency and the simulation's sample period) is in general so small that it is reasonable to consider the channel stationary (unchanged) for the period of a data symbol. Since Doppler shifts encountered in plant applications are unlikely to exceed 50 Hz (corresponding to a Doppler velocity of roughly 6 m/s or 13 mph with a 2.45-GHz RF carrier), their effects are very minor at normal bit rates of 10 kb/s or higher. Nevertheless, to retain validity in general outdoor large-area environments, they are included in the model for completeness and overall accuracy. In the ideal case, with the ray-tracing method of propagation modeling as implemented by Wireless InSite, the actual Doppler velocity vectors (based on the directions of relative motions) may be utilized to calculate the inner (dot) products for each path segment offline to find the precise value of Doppler shift for each; for multiple-reflection paths, the composite Doppler values can then be computed and inserted into the respective branches of the multiple-fingered propagation model. Often,

however, such detailed calculations may not be necessary to obtain a suitably accurate estimate of the overall channel performance for most urban and industrial wireless applications.

According to the paper by Jakes [6], the Doppler-induced modulation of the signal spectrum is given by

$$S(\nu) = \frac{1}{\pi f_d \sqrt{1-(\nu / f_d)^2}}, \qquad |\nu| \le f_d, \tag{3.8}$$

where f_d is the maximum Doppler frequency, which is ratio of the velocity of the mobile v and the signal wavelength λ.

$$f_d = \frac{v}{\lambda}, \tag{3.9}$$

Fig. 3.3 shows the power spectral density of the received RF signal due to Doppler fading. It can be seen that the value of $S_{E_Z}(v)$ is infinite at f=$\pm f_d$. This is not a practical problem since the angle of arrival is continuously distributed and the probability of components arriving at exactly these angles is zero [3].

The spaced-time correlation function $R(\Delta t)$ defined as in [7] is the inverse Fourier transform of $S(v)$, which has the form

$$R(\Delta t) = F^{-1}(S(v)) = J_0(2\pi f_d \Delta t), \tag{3.10}$$

where J_0 is the zeroth-order Bessel function of the first kind.

The correlation functions for different fading rates f_dT are illustrated in Fig. 3.4, wherein the fading rate is the Doppler frequency normalized by the data symbol rate. The results are consistent with expected values since smaller the fading rate is, more slowly the correlation function of the channel varies.

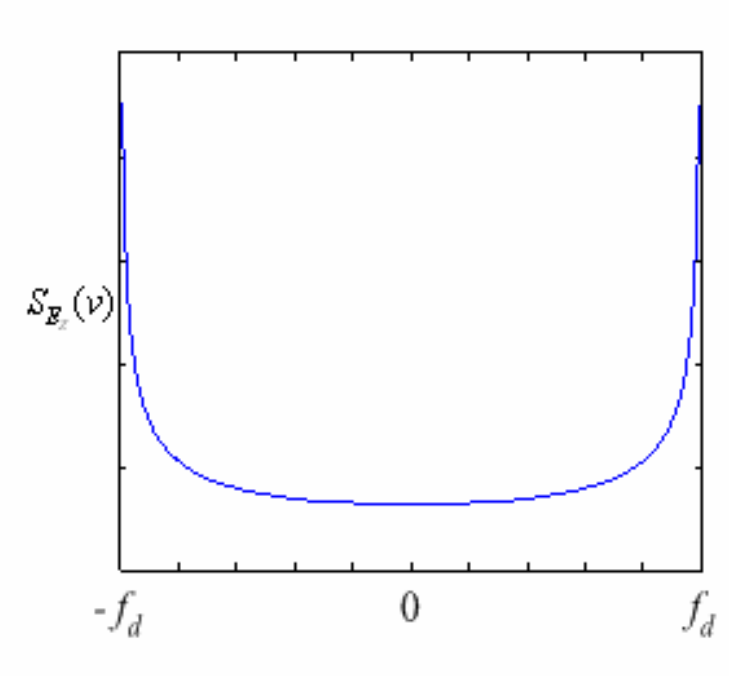

Fig. 3.3 Doppler power spectrum.

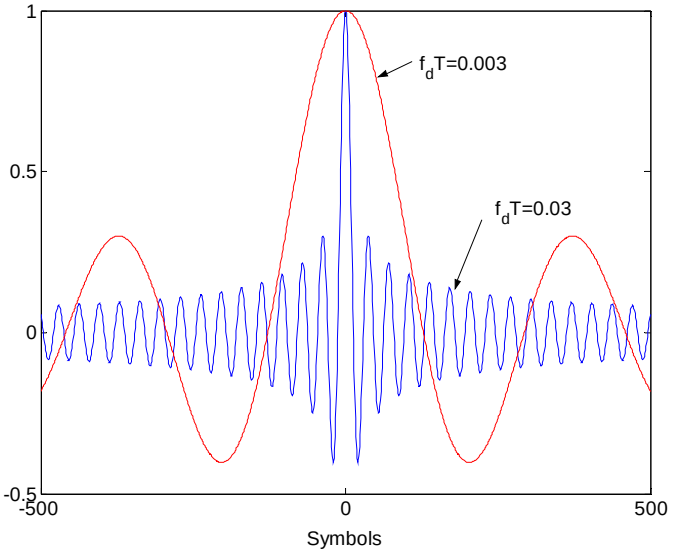

Fig. 3.4 Space-time function in terms of fading rate.

3.2.1.2.2 Frequency correlation- Power-delay profile

According to different channel-dependent relationships between the coherence bandwidth f_0 *vs*. the baud rate R_s, an RF channel can be classified as flat fading or frequency-selective. The coherence bandwidth is reciprocal to the maximum delay spread T_m; that is, the delay between the first and the last component of the signal during which the received power falls below some threshold level (e.g., 20 dB) below the strongest component. Thus the two degradation criteria are:

1. A channel is said to exhibit frequency-selective fading if $f_0 < R_s$ or $T_m > T_{sym}$. In this condition the multipath components extend beyond the symbol duration, which causes inter-symbol interference (ISI) distortion in the signal.

2. A channel is said to exhibit flat fading if $f_0 >> R_s$ or $T_m << T_{sym}$. In this case there is very little ISI.

For the indoor industrial environment, the multipath-induced delay spread is often highly dense and thus the signal will experience serious frequency-selective distortions (i.e., notches in the channel frequency response).

3.2.2 Completely Deterministic Channel Modeling

Deterministic modeling, on the other hand, is realized by applying accurate representations of Maxwell's equations to the propagation environment. It can provide a physical insight into the actual propagation characteristics, based on various physical RF wave-interaction mechanisms. The detailed description and equations in terms of various coefficients of reflections, refractions, diffractions and scatterings are presented in [1], [8].

The main types of deterministic methods are subdivided into two large groups: full-wave methods and asymptotic methods. The first group consists of integral and differential equations and their corresponding series representations, while in the second group the main methods are physical and geometric optics. In the geometric-optics method, three

approaches have been traditionally used: the image-source method, ray tracing and beam tracing.

Ray-tracing algorithms can be implemented in either two-dimensional (2-D) or 3-D forms and have been used to achieve generally good agreement with propagation measurements for site-specific predictions. Available ray-tracing procedures often must handle a large number of reflections and multipath transmissions and hence become time consuming and computationally inefficient. Moreover, large databases of the system operating environment are required, and the parameters cannot be easily changed. Thus, the ray-tracing technique is often not suitable for system simulations which need to be rapidly adaptable and site-independent. Considering all the drawbacks and strengths of the different types of modeling methods, a combination of deterministic and statistical modeling methods is expected to provide better performance in accounting for dynamic variations in the characteristics of the propagation channel. With this in mind, we propose a new model in Section 3.3, which provides the desired accuracy for realistic indoor environments and allows statistical deviations derived from EM-based ray tracing results at the same time. In the following, the evolution and common algorithms for both these two methodologies are discussed.

3.2.3 Hybrid Modeling

Since both deterministic and statistical methodologies have individual disadvantages and advantages, some researchers have proposed to combine these two methods and develop a hybrid propagation model, which presents statistical characteristics based on the fixed values or parameters obtained by the completely deterministic channel modeling tools, so that this kind of channel models might integrate the positive aspects of both. Our model proposed in Chapter 4 is a form of such a hybrid model, and will be discussed in detail later.

3.3 Geometric Optics (GO)-based Modeling

The basis of the channel modeling using the GO approach is a database of the propagation environment, which usually consists of a list of walls associated with material properties for their surfaces, building dimensions, and the deployment of furniture, windows, doors and the like. In a word, an extensive description of the site-specific environments is required before path tracing and power calculations can proceed. Further, some simplifications can be done for the data structure of the database to save much of the computational load for the modeling tool. In [19], it is pointed out that the simulation errors in a ray-tracing simulation are composed mainly by propagation modeling errors, database errors and kinematical errors. The full explanations for each of these can be found in [19].

3.3.1 Ray Tracing Method

There are two basic types of ray tracing methods: two-dimensional (2-D), and three-dimensional (3-D). 3-D ray-tracing methods can handle any kind of RF propagation environments, but need detailed 3-D information of the building and long processing times. On the other hand, 2-D approaches ([7], [11], [13] and [15]) will be practically valuable to avoid time-consuming computations in some simple and regular urban environments. In addition, the 2-D representation can be extended to full 3-D models if irregular scatterers or obstacles are present in the propagation paths.

3.3.1.1 Image-Source Method

Image-source methods compute specular reflection paths by considering virtual sources generated by mirroring the location the transmitter over each polygonal surface of the environment. The key idea is that a direct path from each virtual source has the same directionality and length as a specular reflection path. Thus specular reflection paths can be modeled up to any order by recursive generation of virtual sources. This method is simple for rectangular rooms. However, in general environments, the number of virtual sources required can be large. Moreover, for every new receiver location, each of the

virtual sources must be checked to see if it is visible to the receiver, since the specular reflection path might be blocked by a polygon or intersect a mirroring plane outside a polygon. As a result, this method is practical only for computing very few specular reflections from a stationary source in a simple environment. Usually, the image source method is accompanied by a 2-D approach or the ground-reflection method of ray path generation.

McKown and Hamilton [2] presented the use of quasi-optical ray tracing as a tool for predicting the multi-path propagation of RF signals on a site-by-site basis in urban and indoor scenarios, as a means of avoiding the greater effort, time, and cost of exhaustively solving Maxwell's equations, particularly given the complexity of typical room and building boundary conditions. Ray tracing approximates the scattering of electromagnetic waves by simple reflection and refraction calculations, and thereby obtains much higher accuracy than conventional statistical measures such as spatially averaged "power laws" based on range. The models presented are based on specular approximations to the power-delay profile where walls, floors, and ceilings are presumed to be perfectly flat surfaces along one of the Cartesian coordinate axes; further, all scatterers are assumed to be well separated from the source, large compared with a wavelength, and completely smooth. The rays are ordered in terms of the number of reflections (up to six) to help reduce the computational burden, which was actually implemented (in hours) via a fast workstation using an image-based, dual-grid (small/large to reduce the complexity of the model's reflection geometries), scalar, coherent ray-tracing program to generate planar maps (slices) of 3-dimensional standing-wave patterns for continuous wave illumination. The results are generally useful but not nearly as accurate as a full wave-boundary model such as used in Wireless InSite.

Laurenson, Sheikh, and McLaughlin [9] discussed the use of ray tracing for characterizing indoor mobile radio propagation and demonstrate that even in highly reflective indoor environments the statistics for the fast-fading (highly position dependent) signal-amplitude profiles are not Rayleigh but rather follow a good fit to a Nakagami distribution. The technique described is essentially an image type, which assumes that all

surfaces with roughness dimensions < ⅛λ can be considered as smooth reflectors; also, edge diffraction effects are ignored in the analysis. The rays were computed and their powers determined at multiple points defined by the average over roughly 8-m square blocks. The resulting spatial power profile of a small block of offices in a moderately large building was found to be usually within about 3 dB of the measured values, with some local perturbations approaching 10 dB, especially close to the transmitter. The overall simulated and measured indoor channel amplitude statistics show good agreement with the general Nakagami propagation pdf curve shapes, though the simulated distribution has a peak value of 1.33 and mean of 1.0, while the measured curve fit has a peak of 1.0 and mean of roughly 0.7.

Valenzuela [10] contrasted the previous two papers ([9] and [12]) by predicting the local mean of the received RF power at each point as the scalar sum of all the arriving multipath components. For each path, the loss (in excess of the free-space factor) is calculated as the product of the squared-magnitude of the reflection and transmission coefficients and both antenna patterns. The net reflection and transmission coefficients for each scatterer from a multilayer dielectric model, including angle and polarization effects; an arbitrary number of surfaces are accommodated. The optical-type rays are traced out from the transmitter to the receiver according to the geometry of the indoor environment, using an arbitrary number of reflections from solely orthogonal surfaces. The predicted versus measured signal values are somewhat high due to the assumption of perfectly specular (smooth, lossless) reflections. Although the approach described is conceptually similar to most other ray-tracing techniques in the literature, the author unfortunately does not disclose any significant details of the actual algorithms employed.

3.3.1.2 Ray Launching Method

Based on the ray launching methods [12]-[19] propagation paths between a source and receiver are found by generating rays emanating from the source (or receiver) position and following them individually as they propagate through the environment. Although

this method is very general and simple to implement, it is subject to aliasing artifacts, as the space of rays is sampled discretely and can thus be spatially undersampled.

Walfisch and Bertoni [12] developed a systematic method of accurately predicting UHF radio propagation (e.g., cell-phone signals) in a built-up urban environment by a combination of standard spreading-loss and diffraction factors[1]. This was done by examining the propagation of ray paths from an elevated transmitter site (i.e., base station) through an urban zone outside of the high-rise districts typical of residential neighborhoods, commercial, and light industrial areas, where medium-height buildings (i.e., a few floors) are spaced at regular intervals along streets. These structures serve as multiple diffraction sites to the RF waves and were modeled as a recurring set of cylindrical obstacles, so that an accurate estimate of the propagation losses was obtained by observing that the predominant RF path was along the rooftops, with the subsequent propagation to the street level due to diffraction over and around the buildings. Successive diffractions (modeled as multiple knife-edge diffractions past a series of half-screens) occurred as more buildings were traversed by the propagating base-station signals. The computations were handled via numerical evaluation of the Kirchhoff-Huygens integral, more often employed in the field of wave optics. The overall path losses in the model were found to have a range dependence of $R^{3.8}$ for low transmitting antennas, which was within a few dB of the actual measured field strengths at 820 MHz in the urban environment of Philadelphia, PA.

Honcharenko, Bertoni, Dailing, Qian, and Yee [13] conducted a study of the physical mechanisms defining UHF propagation on single floors in office buildings using typical modern construction techniques. A key feature is the clear space between the ceiling and furniture or floor, which usually contains multiple irregular features such as light fixtures, pipes, conduits, support beams, and the like. These items cause significant diffuse scattering of the propagating signal and can cause local losses significantly in excess of the normal R^2 distance-spreading loss experienced by direct and specularly reflected components bouncing off flat walls, floors, and such. This excess path loss can be closely modeled by calculating the successive signal diffractions caused by a series of absorbing

screens near the main RF propagation path, much as detailed in Walfisch and Bertoni [12] above. Diffraction around corners and through external windows (and back inside) is also a major consideration in evaluating the fields near obstacles, and may also be the major contributor to the total field when strong direct or reflected paths are absent. The slightly diverging rays used in the model are used to compute a sector-average signal, which is carried forward as many times as required to complete the simulation of the complete transmitter-to-receiver ray path and estimate the final received ray power at the receiver; the final power is simply the sum of the powers of the valid rays. With typical hallway-centered, longitudinal building layouts, the predicted fields using geometric ray-tracing methods were within 2-3 dB for hallway locations and within roughly 3-7 dB for room-to-room paths. An average regression for short halls gave an $R^{1.7}$ function, due to the wave-guiding effects of the hallway walls; a range dependence of about $R^{3.7}$ was observed for receivers in offset halls and individual rooms and/or offices up to a distance of 60 m.

Lawton and McGeehan [14] presented a prediction algorithm to estimate the propagation characteristics for small-cell (i.e, with a radius ≤ 150 m), high data-rate systems using geometric optics and the geometric theory of diffraction. The technique launches rays to evaluate reflected, transmitted, and diffracted daughter rays, including internal media refraction effects, using a database of typical values of permittivity, permeability, and conductivity for several common wall materials, glass, and copper sheeting. The calculations are performed using standard optical formulas including Snell's law; the multiple rays generated at each surface interaction are combined into a single transmitted and reflected ray, which is carried forward in the model. The algorithm proceeds by reflecting the transmitter about permutations of the reflecting walls and calculating the corresponding transmitter images. Information about these images is subsequently stored in an array and used for all receiver locations. For each receiver, connecting lines are then drawn between the transmitter and receiver images; for lines intersecting only reflecting walls, a purely reflected path results, which is evaluated for delay, attenuation, and phase, with some adjustments for diffraction effects. The output of the model is a plot of overall

RF delay spread for the specified environment, which in most of the depicted test sites gave reasonably good agreement to channel-sounding measurement values.

Kreuzgruber, Gahleitner, et al [16], [17], described a fast search algorithm for a ray-splitting propagation model that provides a simplified means of adjusting for the effects of edge diffraction and diffuse scattering from rough walls. Scattering sources of non-specular reflection are represented by new radiation point-sources. In the new ray-splitting method, a field tube of rays, emanating from a source, is cut into finite-length parts, each of which terminate at a zone bound, where a change in the propagation medium exists or where the tube end diameter is doubled from its starting value. At its end the tube is split into a group of 4 tubes. The assembly of consecutive rays forms a ray path, which terminates when: (a) the number of permitted zone bounds is exceeded; (b) the maximum number of reflections or transitions is exceeded; or (c) the path loss exceeds a predetermined limit. Each ray is characterized by an electric field vector and an equivalent delay due to the length of the path. When a ray tube intersects a boundary or diffracting edge, it is replaced by a new ray, which either consists of a reflected/transmitted pair or a diffracted-ray source, whose power is adjusted according to the interaction loss and phase. If the ray power at any point in the progressive process drops below a set value, the ray is eliminated from the ensemble calculation. Beyond a few meters from the transmitter, the simulated and measured received-power values are consistently within about 3 dB, verifying the accuracy of the ray-splitting methodology.

Wagen and Rizk1 [18] described a ray-tracing method for predicting RF channel impulse responses in urban-microcell areas, particularly where line-of-sight (LOS) paths may quickly change to non-LOS when a mobile unit rounds a corner or passes behind an obstacle. The authors argue that although specular reflections can explain some propagation effects, scattering must also be considered to accurately model the rapid spatial changes in channel characteristics. For given transmitter and receiver locations, all possible rays combining reflection and diffraction up to a fixed order were traced, and for each ray the complex amplitude and delay were calculated. A nominal 3-dB loss for each reflection was assumed. Two test cases were considered, one a 2-corner street

intersection and the other a 4-corner scenario. The application of ray-tracing calculations produced fairly good estimates of the overall path attenuations near the 4-corner spot, but the prediction of the 2-corner intersection losses and impulse response showed significant deviation from the measured values. The most likely cause was stated to be the existence of significant scattering by nearby trees and a large metal fence, which warranted further investigation.

Durgin, Patwari, and Rappaport [19] described a new 3-D ray-tracing technique of high speed and accuracy to improve the quality of RF propagation predictions over the usual statistical methods. The paper focuses on three major ray-launching concepts: (1) geodesic ray launching; (2) improvements in the reception-sphere concept from the previous literature; and (3) a new method for interpreting ray information using a special weighting function to construct ray-traced wavefronts. The use of a geodesic sphere permits ray launch points at the vertices with equivalent angular separation between neighboring rays around the entire sphere, thus providing a nearly uniform angular ray distribution to probe the propagation volume. Aberrations in real polyhedral shapes are generally small and can be easily compensated. The concept of a reception sphere is exact in 2-D cases but can be ambiguous in 3-D. The instance of double-counting rays can give 2:1 power errors, so the use of *distributed ray wavefronts* can eliminate these problems by weighting the incoming rays in the field computations according to their proximity to the receiver. The algorithm inherently filters out rays that do not have an unobstructed path from the receiver location and the ray's source (either transmitter or surface intersection). Diffraction effects were mentioned but not included in the disclosed technique. Results of simulations versus measurements were within about 1 dB for total power and reasonably good for the environment's time-delay profile.

Yang, Wu, and Ko [20] developed a modified ray-tracing procedure to model specifics of propagation and penetration of indoor RF waves around several types of complex interior structures, including irregular rooms and stairwells of multiple material types. The geometrical optics-type rays were traced not only by including the multiple reflections and transmissions inside building boundaries but also inside the material structures; each

ray was represented by shooting 4-ray tubes based on the antenna patterns and evaluating the spreading factors of the ray tubes. Each of the rays in the tube formation is spaced by a spherical heading angle of roughly $\theta/\sin\theta$, where θ is typically 1 to 3 degrees. This approach permits some spatial averaging in the E-field values; in each instance, the complex dielectric coefficient, which includes the real losses, is used for evaluating the fields in each of the scattering and transmitting media. To accurately model the spreading of the tubes reflected or transmitted through the complex structures, the ray tubes are traced and the cross-sectional areas of the tubes are computed at the receiving locations to derive the effective spreading factors based on the conservation of flux in a ray tube. Using this technique, wave behavior in electrically large 2-D and 3-D structures was analyzed. A 2-D moment method was used to verify the accuracy of the ray-tracing approach for test cases of an RF line source illuminating a two-room space and through a stepped-thickness lossy-dielectric wall above a lossy ground plane; the ray-tracing results showed good agreement with the moment calculations for both instances. Further measurements of internal hallways and in stairwells of a large, multi-story building confirmed the ray-tracing simulation models within about 3-5 dB in most cases, with a few points off by about 10 dB closer to boundaries. The simulations ran within 1-4 minutes on a Pentium-166 machine, with measured dielectric-constants employed for the various materials in the structures.

Another, more interesting ray-tube tracing method was developed by Son and Myung [25] to predict RF propagation in the downtown core area of Ottawa, ON. This very fast ray-tracing tree algorithm is based on the uniform geometrical theory of diffraction and outperforms many other ray-tracing methods. It has been applied to quasi 3-D environments and in a complex urban layout with arbitrary-shaped buildings and streets, by finding all possible propagation paths from a transmitter to a receiver using a point-to-point tracing method based on the image concept which offers good computational efficiency. The method described defines three types of ray tubes (spaces containing potential rays) – transmitter, reflection, and diffraction – which are developed from site-specific information on the plane view of the quasi 3-D environment. The transmitter ray

represents a bundle of rays from the transmitter and is characterized by the transmitter's location and the tube angle (azimuth) of a full 2π radians. The blockage of this tube generates daughter reflected and diffracted rays, which in turn are represented by new ray tubes. The reflection ray tube is the bundle of rays reflected by a wall or other surface and is described by the position of the image on the wall, the wall number, and a tube angle < π radians. It generally has a fan-like shape but its valid region is limited by the wall structure around the reflection point. The diffraction ray tube consists of the family of rays diffracted by corners and is described by the position of the corner, the corner number, and the tube angle, which can in general exceed π radians. For the typical complex environment, a tree ray-tube structure can be constructed from site-specific data. Unlike conventional image methods, the predefined ray tubes embed information about their apexes, angular extents, and valid regions, which also permit easy generation of daughter tubes from the same site data. In the analysis, tubes with very high loss (~150 dB) are discarded. After all the ray tubes are sifted, the 2-D propagation paths thus specified can be converted to 3-D ones, largely to handle ground reflections. Finally, the fields for each path are calculated and vectorially summed at the receiver point. Since the method handles reflected and diffracted bundles identically, the process of site analysis is greatly simplified. As diffractions up to 10^{th} order are included, the ray field data is quite accurate. The modeling predictions were mostly within 3-5 dB for path loss; delay spreads are also close to measured values.

Ji, Li, Wang, Chen, and Sakar [21] provided an improved-efficiency algorithm for two-dimensional ray-tracing propagation prediction for indoor RF signals by reorganizing the scattering objects into irregular cells which are used to exclude areas in which no ray interactions occur. The cells are formed by concatenating multiple boundaries (line segments) into either new lines or segments which describe the diagonals of an enclosed area (box). If the RF ray in question does not intersect the new line or box diagonals, then the feature can be deleted from the calculations of the fields for those missing intersections, thus saving close to 60% of the traditional complete-room solution time. Since no ray intersections with true objects are omitted, the results are still as accurate as

with conventional exhaustive-search techniques. A simplified 3-dimensional (3-D) ray-tracing approach results from projecting all walls, objects, the transmitter, and the receiver vertically on the floor, using the 2-D approach on the projection plane to simplify the problem by eliminating the non-connecting paths between transmitter and receiver. By relating the projected 2-D paths to the possible ensemble of 3-D paths, an even larger proportion of possible 3-D paths can be dropped from the calculations, thus saving even more operations; compared with standard full 3-D ray calculations, the new algorithm can reduce the time to about 1% of the usual amount. Signal measurements in an indoor area have confirmed the accuracy of the method to be close to that of the full 3-D approach (within a few dB of the measured values).

3.3.2 Beam Tracing Method

Beam tracing methods proposed by Fortune find propagation paths from a source by tracing beams (i.e., bundles of rays) through a 3-D polyhedral environment, In general, a set of beams is constructed that completely covers the space of rays from the source. For each beam, polygons are considered for intersection in order from front to back. As each intersecting polygon P is detected, the original beam is clipped to remove the shadow region. Additionally, new beams may be created representing various types of propagation mechanisms: reflection, transmission, diffraction and refraction.

S. Fortune [27] of AT&T Bell Laboratories described a beam-bouncing algorithm for predicting indoor RF propagation using a triangulation-based data structure to achieve fast simulation speeds for large buildings. In the technique, each wall in the room can be viewed as a partially reflecting mirror that illuminates a polyhedral cone using power reflected from the base of the cone. If a sample point lies within a cone of illumination, there exists a propagation path to the sample point reflected off the corresponding wall; the actual path power is often reduced by the shadowing of intermediate walls. With these illumination cones, all propagation paths can be found, up to a fixed number of reflections. The algorithm employs a spatial data structure based on triangulations to map the paths. The technique has fast, even response and permits rapid detection of all

obstacles that lie in a polyhedral query cone. The beam-tracing technique is close to ray-tracing in performance but has fewer sampling artifacts. Essentially, the algorithm operates as follows: with a fixed transmitter location, the reflection cone for a wall *w* consists of all points reachable by a single reflection off *w*. If *v* represents the reflected image of the base of the cone in the plane of the wall, *v* is a virtual transmitter. A sample point is reachable by a single reflection off wall *w* if the line segment from *v* to the sample point intersects *w* at the reflecting point. Thus the reflection cone is a truncated polyhedral cone, with apex *v*; each plane through *v* and one of the edges of *w* bounds the cone, and the cone is truncated by the plane of *w*, removing the part of the cone from *v* to *w*. Recursively applying this procedure, the possible paths are determined, with a great savings in operations (up to 30×) due to the pruning of non-valid cone regions. The algorithm has also been incorporated into a commercial modeling tool called WISE.

3.3.3 Ray-Beam Tracing Method

Due to the disadvantages and advantages of both ray-tracing and beam-tracing algorithms, some researchers proposed to combine these two methods in two steps. If beam tracing is implemented first one would divide the whole space into a few or a small number of scattering portions, next a ray-tracing algorithm is used to refine the results, which was proposed in [28]. An alternative approach is to switch the order of these two algorithms, which was presented in [31]; after implementation of the ray-tracing algorithm, the beam-tracing algorithm is used to improve the results by reducing the sampling error introduced by the ray-tracing processes.

Rajkumar, Naylor, Feisullin, and Rogers [28] presented a variation of standard ray-tracing to predict RF propagation in site-specific environments, termed *ray-beam* tracing. To accomplish this, the geometric environment is represented in full 3-D, using broadcast signal propagation to analyze both indoor and outdoor venues. Simple ray tracing has a major disadvantage in that adjacent rays from a transmitter diverge significantly after long distances, thus increasing the size of the analysis regions. This problem is countered by adopting the notion of a beam, while maintaining the simple ray technique for

intersection determinations. The beams are adaptively split into daughter beams to limit the sampling error in the region of interest. In this system, the geometric environment is represented by constructing a "partitioning tree" which defines the spatial relationships between polygonal surfaces and encodes these relationships in a set of binary trees, which in turn are built by recursively subdividing 3-D space by planes to create successively smaller spatial regions. Thus, following a path deeper into the tree corresponds to adding more detail, thus producing a multi-resolution spatial model, with more detail where it is needed. This in turn yields a more efficient intersection computation for propagation estimation as well as for scene visualization. The space is thus partitioned into regions either totally inside or outside objects, permitting rapid sorting of the spaces for computation. Further, the system can represent both very coarse and very fine detail within the same data structure, with major efficiency gains. Applying the technique to very complex areas of downtown Manhattan, the model produced mean errors of only 2 dB, with standard deviations of 5-8 dB, compared with field measurements.

Chapter 4

Proposed Channel Model

A generalized site-specific propagation model, based on geometrical ray tracing, with modern computers is now computationally feasible to predict details about a specific site with known parameters such as geometry and building materials. This general model can be used to develop a suitable site-specific version by adjusting the specific parameters of the various physical paths. The model needs to be sufficiently general to include signal properties such as polarization, correlation, coupling loss, and channel parameters such as geometry, Doppler-shift, dielectric constants so forth.

Motivated by these facts, we propose a site-specific channel modeling for industrial, reflection-rich environments. Coherent ray tracing can approximate the scattering of the incoming signal by incorporating the simple multiplication of reflection, diffraction and refraction effects using practical simulation runtime, whereas fully solving Maxwell's equations for the propagation environment or field RF measurement campaigns are tedious. First, we propose our general propagation model including cross-polarization coupling. We investigate the validity of our model using commercially available EM modeling software tool, Wireless InSite [1]. We will restrict our attention to a detailed yet general propagation model, which is not only specific for the industrial environment, but also can be applied to many other indoor and urban settings.

4.1 Proposed Model

In the preceding chapter we looked at the characterization of multipath channels from both the traditional statistical and deterministic viewpoints respectively. As discussed previously, ray-tracing (RT) is one of the most popular techniques for predicting radio channels used in deployment tools. The main characteristic of RT is its computational intensity, which is the main reason for the prediction tools to be computationally slow in spite of its accuracy. This has motivated a significant research effort to pursue alternative

methods including the so-called Fast RT, in an attempt to expedite the computation times. Still, these alternative methods require a more complex floor-plan database and the need to trace all rays regards of their significance to the receiver power.

In this chapter, we will present in detail the proposed new channel propagation model and then explicitly specify the model structure and its means of implementation.

4.1.1 Structure of the Channel Model

According to Eq. (3.6) in the previous chapter, the channel lowpass-equivalent output is given by:

$$\tilde{y}(t) = \sum_{k=0}^{L} \tilde{c}_k(t) \cdot \tilde{s}(t - \tau_k). \tag{4.1}$$

We also discussed the polarization effects the channel introduced through reflection, diffraction and scattering mechanisms. In order to incorporate the polarization rotations observed for vertical, horizontal polarized or dual-polarized antennas, the output signals need to be divided into horizontal and vertical components, which can be expressed as

$$\begin{cases} \tilde{y}_V(t) = \sum_{k=0}^{L} \tilde{c}_{kV}(t) \cdot \tilde{s}(t - \tau_k) \\ \tilde{y}_H(t) = \sum_{k=0}^{L} \tilde{c}_{kH}(t) \cdot \tilde{s}(t - \tau_k) \end{cases}. \tag{4.2}$$

Thus, a more general discrete multipath channel model is derived in Fig. 4.1, which adopts the typical tapped-delay-line structure. Notice that the input, output signal and the tap gain variables are expressed as time discrete expression given by

$$\begin{cases} \tilde{y}_V(k) = \sum_{k=0}^{L} \tilde{g}_{kV}(k) \cdot \tilde{s}(k - \tau_k) \\ \tilde{y}_H(k) = \sum_{k=0}^{L} \tilde{g}_{kH}(k) \cdot \tilde{s}(k - \tau_k) \end{cases}. \tag{4.3}$$

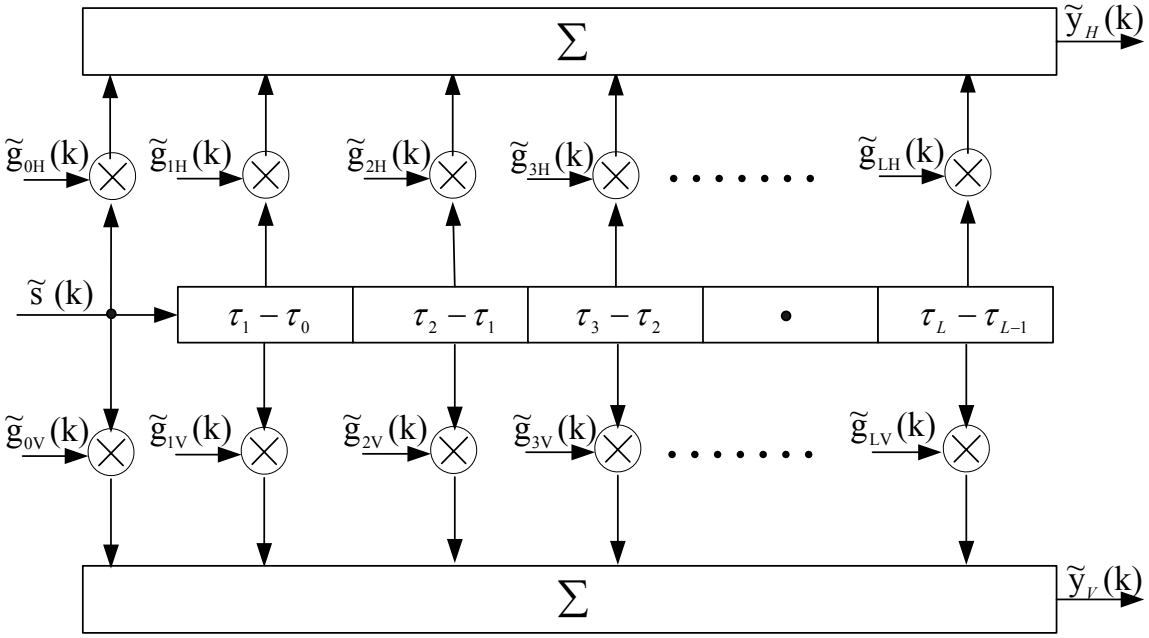

Fig. 4.1 Tapped-delay-line model for multipath channels.

4.1.2 Tap-gain Process Generation

The generation of the tap-gain process for the discrete multipath channel model is straightforward from Eq. (4.3) and is illustrated in Fig. 4.1. As it can be seen, there are (L+1) different versions of input signal $\tilde{s}(k)$ caused by the (L+1) different excess delay, then multiplied correspondingly by the vertical and horizontal polarized components of tap gains of multi-path to obtain the vertically polarized output $\tilde{y}_V(k)$ and horizontal polarized output $\tilde{y}_H(k)$, respectively.

In Fig. 4.2, the tap-gain random process for producing the vertically polarized received signal is presented. The horizontal structure is similar and is represented by exchanging the subscripts V with H in Fig. 4.2. For simplicity, only the vertical case is discussed in this section. We start with a set of (L+1) independent, zero-mean, complex Gaussian white noise processes $\tilde{n}_k(m)$ with correlated in-phase and quadrature components. These

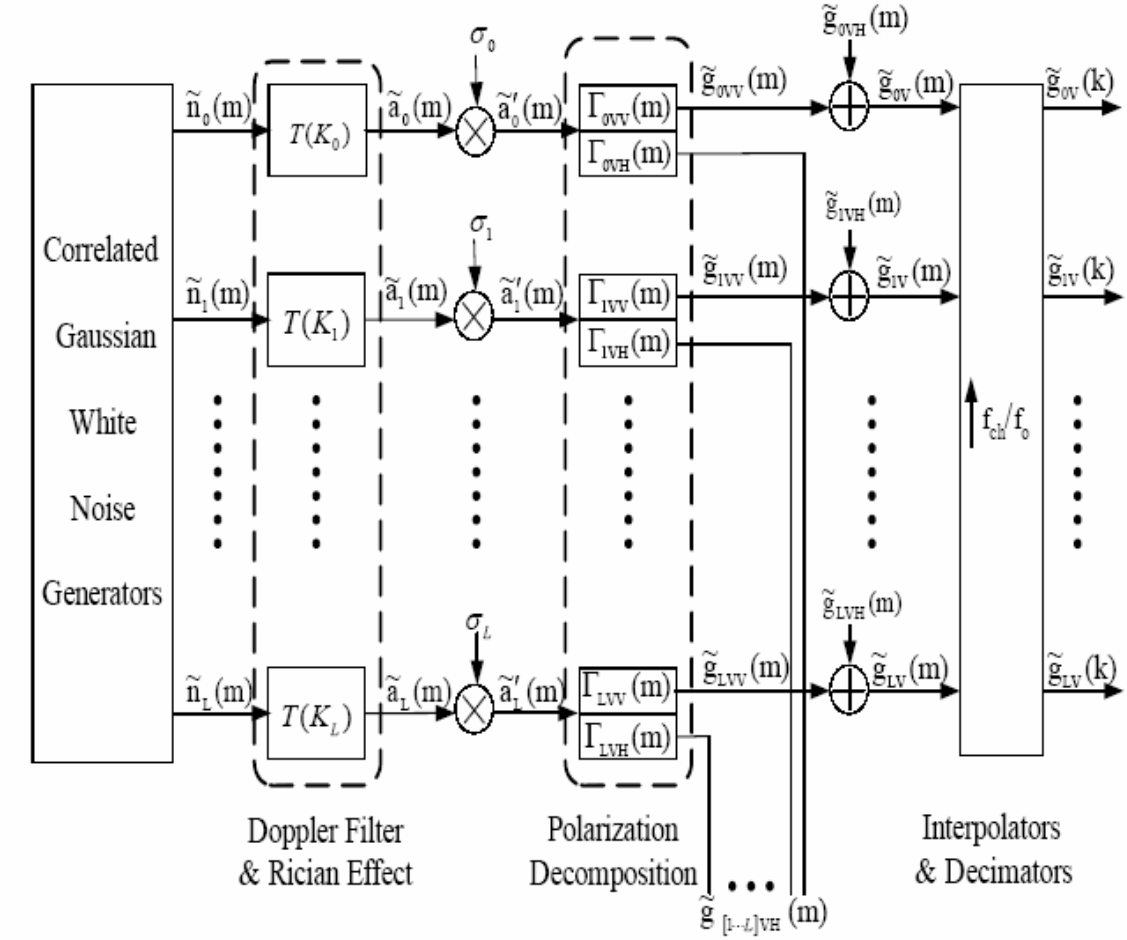

Fig. 4.2 Vertically polarized tap-gain process generator.

are fed into the $T(\cdot)$ transform block to obtain the appropriate Doppler spectrum with Rician effects, then scaled with the σ_k s to produce the desired power level for the *k* paths. To represent polarization effects, the intermediate signals $\tilde{a}'_k(m)$ are multiplied by the horizontally and vertically polarized components of the complex reflection coefficients $\Gamma_{kVV}(m)$, $\Gamma_{kVH}(m)$ respectively to obtain process $\tilde{g}_{kVV}(m)$. Then we combine this with the component from the horizontally polarized tap-gain $\tilde{g}_{kHV}(m)$ to compute the tap gain values $\tilde{g}_{kV}(m)$. For the single sampling-rate system, $\tilde{g}_{kV}(m)$ is the final tap gain value shown in Fig. 4.2. However, in most practical simulation experiments, the intense computational complexity requires applying a multi-rate mechanism in the system performance simulation, especially to facilitate using a lower sampling frequency in the channel model for the sake of running time. Therefore, the interpolation and decimation operations need to bridge the different sampling rates between the channel and modulated-signals data outputted from the transmitter. There are several methods commonly used in digital signal processing to achieve this purpose. Thus, the time indices *k* in $\tilde{g}_{kV}(k)$ are intentionally adopted to differentiate the process $\tilde{g}_{kV}(m)$ coming from the lower sampling-rate channel modeling.

4.1.3 $T(\cdot)$ Transform

In Fig. 4.3, the specific time correlation characteristic is obtained by feed the correlated complex Gaussian noise $\tilde{n}(m)$ into the corresponding Doppler filter H(z). Its transfer function can be expressed as the square root of the Jakes Doppler spectrum, which was previously given by (3.8),

$$H(f) = \sqrt{S(\nu)} = \sqrt{\frac{1}{\pi f_d \sqrt{1-(\nu / f_d)^2}}}, \qquad \textbf{(4.4)}$$

where *H(f)* is the Fourier transform function for the Doppler filter. Two versions of discrete Fourier transform H(z) are derived later in Chapter 5 for two different sampling rate or cutoff frequencies.

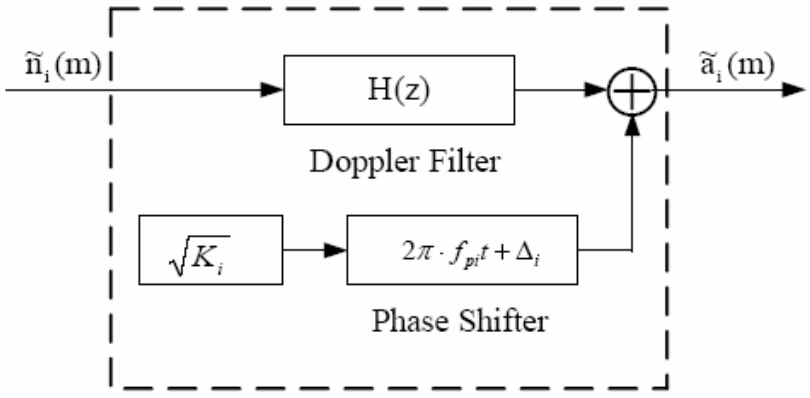

Fig. 4.3 $T(\cdot)$ Transform.

On each path, a dominant component occurs along with a cluster of rays. The Rician-distributed amplitude is expected as described in the previous statistical channel-model discussion. The dominant component in the *i*th path is scaled by the Rician factor $\sqrt{K_i}$, and then passed to the phase shifter to handle the mobility of the TX/RX antennas with Doppler frequency f_{pi} and the reflection-coefficient introduced phase rotation Δ_i.

4.2 Implementation Procedure

4.2.1 Deterministic Stage

For a typical urban/industrial setting, representing a moderately large manufacturing or material-storage area or building, we have depicted an enclosure approximately 30 m wide [X] by 48 m long [Y] and 30 m high [Z], with a divided room about 10 m by 10 m. The origin for the coordinates is at the lower left corner in Fig. 4.4 (b), an overhead view of the area under consideration. The RF transmitter ("TX") is located at coordinates (15, 9, 1.3) and the receiver ("RX") is at (18, 36, 1.3), inside the sub enclosed room. At right, Fig. 4.4 (c) provides a perspective view of the area, with the receiver room enclosed with one wooden wall [light shading], three concrete or sheet-metal walls [dark shading] and

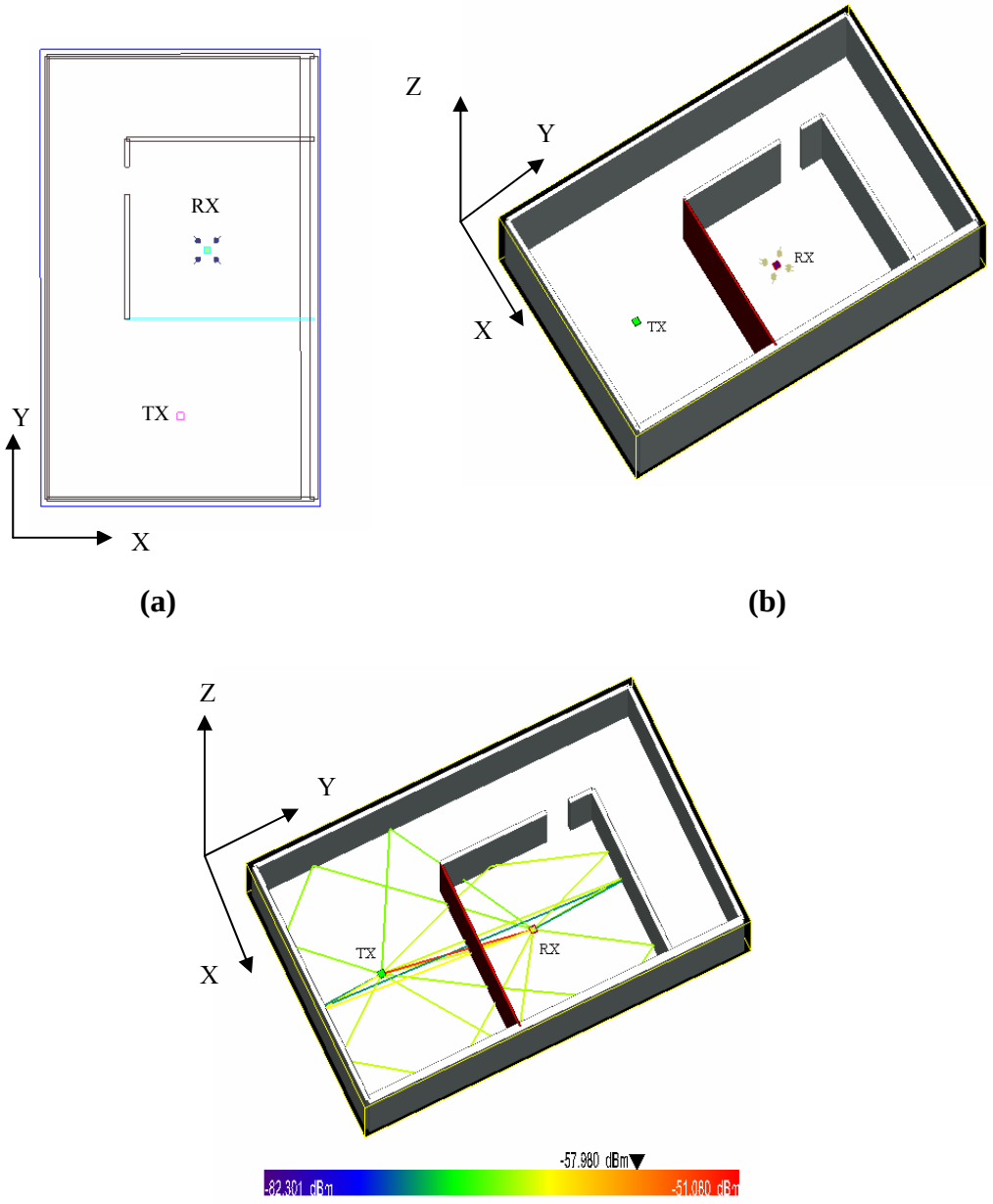

Fig. 4.4 Example RF signal environment, (a) overhead plot of example area, (b) perspective view of area, (c) example RF signal environment with signal paths [32].

concrete floor and ceiling. The main area is assumed to be constructed of concrete-block walls, concrete floor, and concrete ceiling. The plot of Fig. 4.4(c) depicts the RF ray paths from transmitter to receiver, as generated by the Wireless InSite program. Note the direct path between TX and RX through the wooden wall of the sub enclosure. Obviously, the metallic walls of the divided room contribute heavily to the multipath profiles shown, and the effective electromagnetic decay time is significantly increased over that of an all-concrete or other lossy environment.

For the example concrete (Fig. 4.5 (a), Fig. 4.5 (b)) and partial metal-walled (Fig. 4.5 (c), Fig. 4.5 (d)) environments, the overall power-delay profiles of the significant paths (i.e., those with amplitudes within roughly 20 dB of the highest-amplitude path or as defined by the InSite user) are extracted from the InSite case output files and displayed by a custom MATLAB® routine. In Fig. 4.5 (a) at left, the entire ensemble of 30 paths are plotted, with the direct path (at roughly 18 meters) shown at left, along with a closely spaced back-reflection. To reduce the computational time, the path set was parsed via combining paths with similar time bins; the resulting simplified plot with 7 paths is provided in Fig. 4.5 (b). The time resolution for the bins as illustrated in Fig. 4.5 (b) is 10 ns, since the MATLAB system simulation driven by the profile was run with a 100-MHz clock rate, thus requiring a minimum time delay step of 10 ns. Likewise, the case for the metal-walled room reveals similar multiple delayed paths, but the later reflections are less attenuated [Fig. 4.5 (c) and (d)] than in the all-concrete case, as would be expected.

Fig. 4.6 is another example of site-specific environment, which is a typical containment building in NPPs. Compared with the simplified room environment shown in Fig. 4.4, the dome structure is more complex and more realistic. As can be seen in Fig. 4.6, the containment building is generally a circular building with a hemispherical roof structure. It contains the nuclear reactor and two stem generators, which are represented by the cubic and cylinder objects in the figure, respectively. The building also contains large pumps to transport the heated water outside, as well as many other types of auxiliary equipment, including fuel transportation systems, control systems, sprinkler systems,

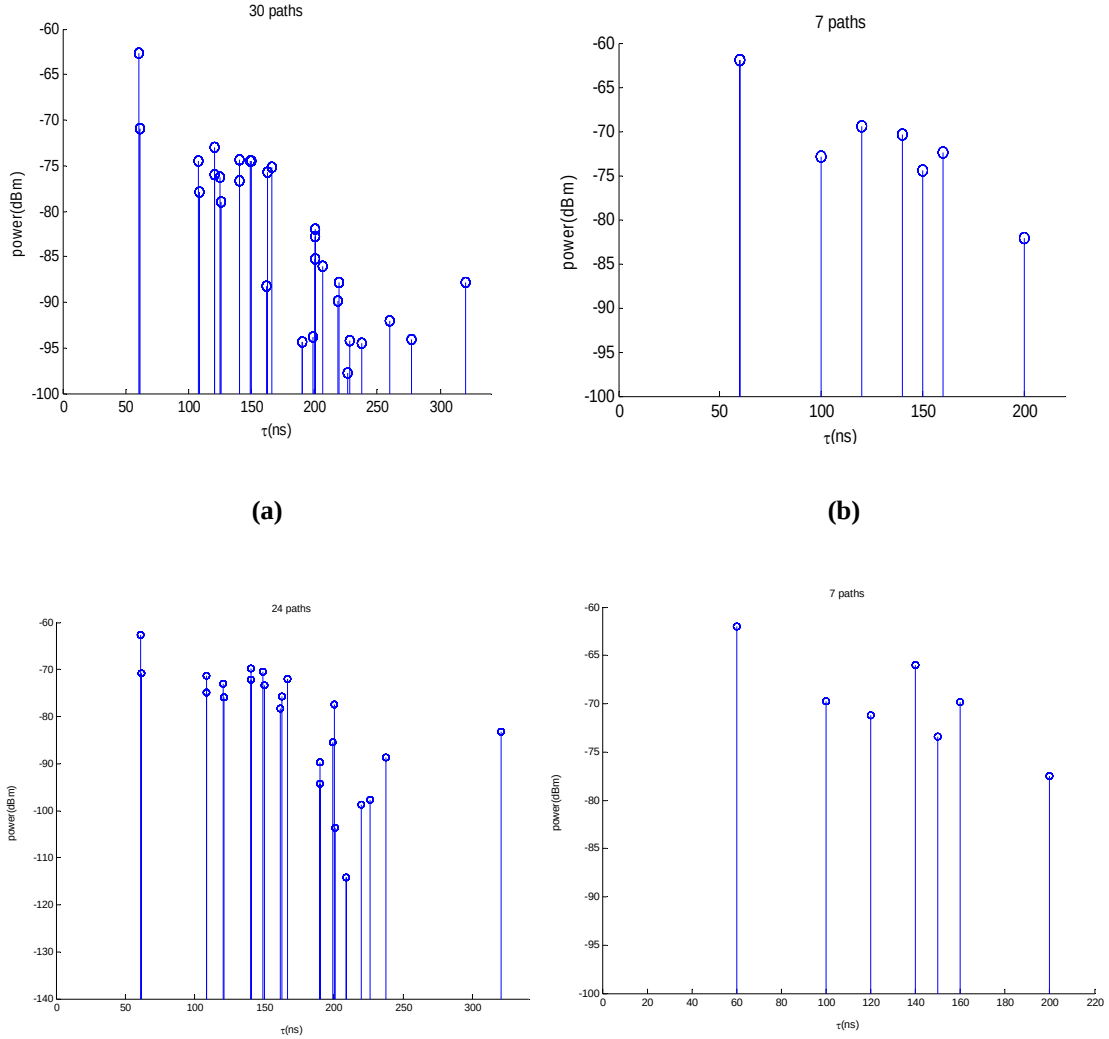

Fig. 4.5 Power-delay profiles of example propagation environment, (a) original path set (concrete), (b) simplified path set (concrete), (c) original path set (metal), (d) simplified path set (metal).

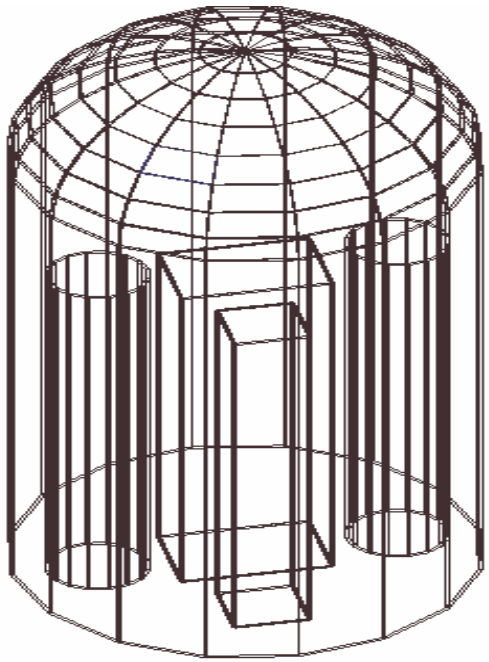

Fig. 4.6 Example containment building in NPPs.

ventilation fans, and a crane for lifting the reactor head, although they are not shown in this figure. However, it is easy to include them in the drawing by using AutoCAD or other commercial software, which can save DXF file.

4.2.2 Interface between the Deterministic and Statistical Stages of the Model Computations

Since Wireless InSite stores the path power, delay and the types and number of signal-boundary interactions in the output file named *project_filename.paths*, an interface program was developed for extracting the power-delay information from this file and importing it into Simulink models for the ultimate channel modeling calculations and system performance measurements.

4.2.3 Statistical Stage

In this portion of the process, the parametric propagation model is developed to permit the desired generality by adjusting the parameters to suit any type of wireless signal network, including its RF environment. First, we will present a simplified model in terms of the parameters exported from our custom-developed interface program, where initially the polarization is neglected. After this straight-forward channel model is implemented by the simulation tools and verified by the link performance results by applying the simulation tolls, we will address the details of the full polarization-aware channel model.

4.2.3.1 Simple Model

The proposed simplified *n*-fingered propagation model is shown in Fig. 4.7, where *each path* is represented as a Rician-type, partially randomized and Doppler-modulated transfer function, characterized by separate gain (amplitude) [G], reflection coefficient [Γ], delay [Δ], and phase [ϕ] terms. A simple Doppler shift (as needed) is applied to the I and Q branches of the direct-signal components, which handles changes in the direct path due to relative transmitter-receiver movements. The notion of a path reflection coefficient, first discussed in [30] for FM radio, offers a useful, measurable way of describing signal interactions with the physical environment. The Rician statistics in the model can be altered as required to fit the environment by adjusting the degree of correlation between the two usually independent Gaussian noise sources; this serves to represent the spatial correlation between the quadrature components due to common spatial interactions such as wall reflections. This, is of course, added to the inherent correlation due to the Doppler shifts in the propagation path, and induced by motion of any transmitter, receiver, or intermediate reflector. The path amplitude, reflection coefficient, and delay terms employed can be reasonably easily obtained by physical measurements in the environment, whereas the path amplitude, delay, and phase parameters are explicitly available as output files from the Wireless InSite program. Eventually, all these may be combined into a composite complex transfer function for the path, if desired. The output signals from the *n* paths are finally summed at the input to the receiver, as shown at right.

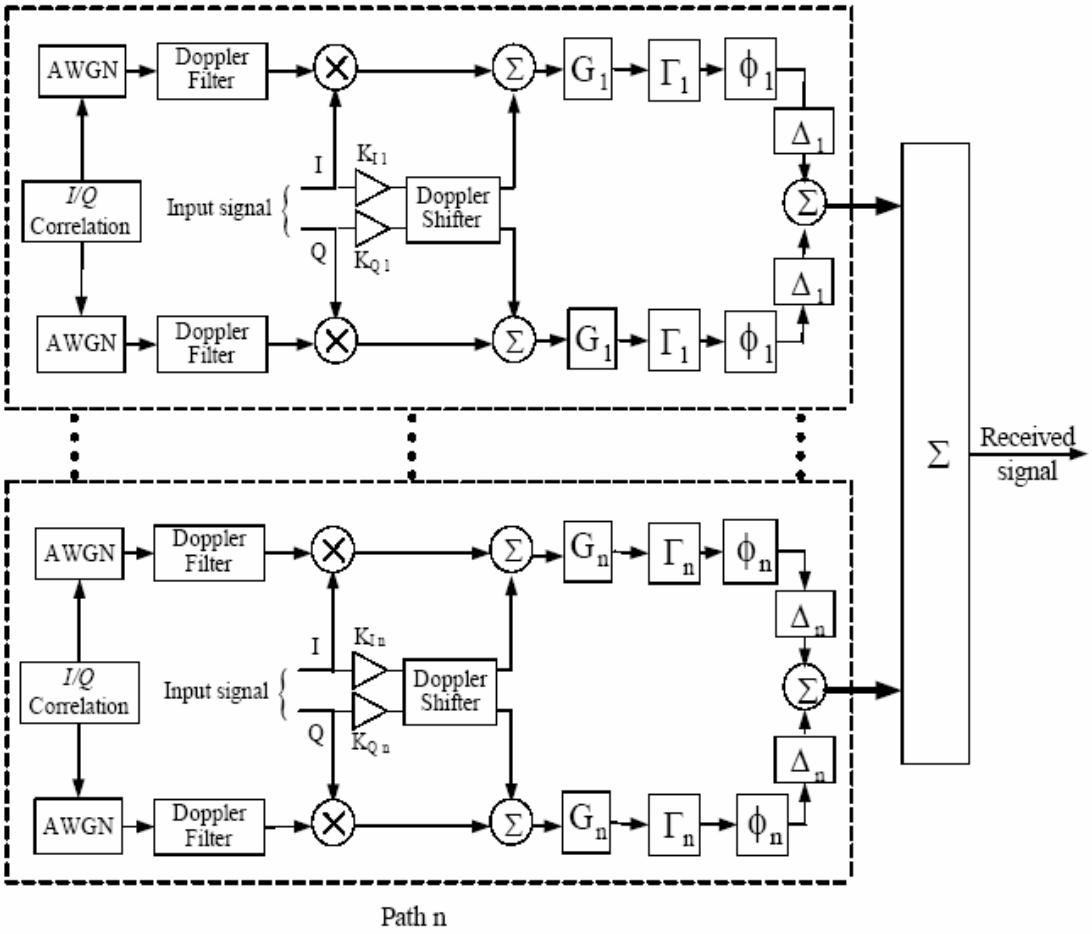

Fig. 4.7 Basic parameterized multi-path propagation model [32], [33].

4.2.3.2 Full Propagation Model

Fig. 4.8 shows a more complex but physically accurate version of the model in Fig. 4.7. Here the basic form of the model is unchanged, but each main propagation path is now modeled as two parallel, orthogonally polarized paths. Each polarization sub-path includes reflection coefficients which represent cross-polarization interactions in the path, where interactions with oblique surfaces and/or anisotropic materials can cause partial rotations of the signal polarization vectors. The statistical interactions between the quadrature I and Q paths are (as Fig. 4.7) defined by the spatial correlations of the RF interactions with the physical environment; the same also holds here for the modeling of the vertical/horizontal (V/H) signal polarizations. The complex 3-D field solver within Wireless InSite can calculate the signal polarization components at each interaction point (e.g., reflection surfaces, diffraction centers, and the like) to ascertain the effective cross-polarization effects on a point-by-point basis as required. The end result is that in modeling a severe multipath environment, we can now accurately determine the extent of signal-polarization rotations induced by the environment and even predict optimum placements for diversity receiving (and even transmitting) antennas for a given locale. Although beneficial for modeling indoor environments, this feature of the model is even more useful in outdoor scenarios where naturally occurring oblique surfaces such as sloping hillsides cause significant cross-polarization conversion in reflected or scattered signals incoming to the receiver. In the model, the reflection coefficients are designated, for instance, as Γ_{nVH}, where the subscripted quantity represents the effective Γ for the *n*th path, for incident vertically polarized signal components which are converted to horizontal output waves by the physical reflection or scattering mechanism in the overall path. Similarly, a Γ_{nVV} term corresponds to a situation where an incident vertically polarized wave emerges from the interaction still vertical; clearly, any degree of polarization rotation can thus be described by the vector sum of the two orthogonal reflection coefficients.

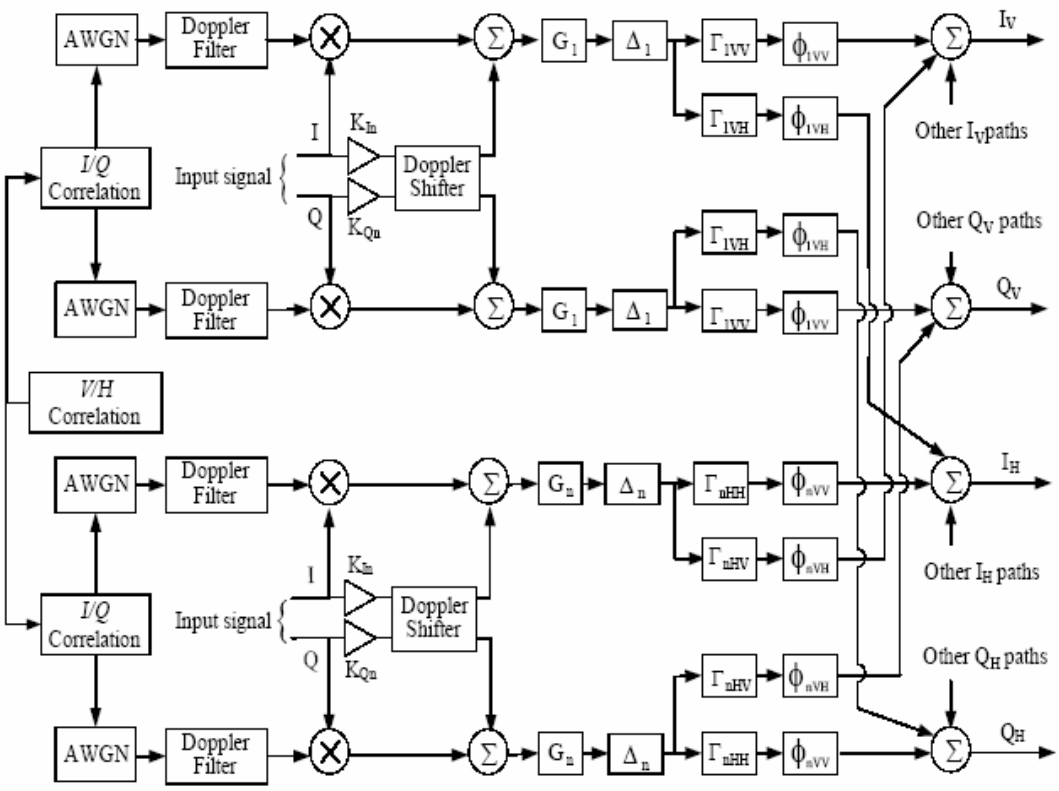

Fig. 4.8 Detailed propagation model with polarization effects [32], [33].

Chapter 5

Simulations and Results

This chapter covers the details and results of the channel simulations for both Bluetooth and Wi-Fi systems, in general (statistical) and specific (semi-deterministic) environments. For the general cases, familiar AWGN, one-path (Rician) and two-path (Rician fading as the direct path and Rayleigh fading as the secondary path) channels are analyzed and bit error rate (BER) results presented. For the specific scenarios represented by wireless InSite, the detailed multi-path models are used in the channel calculations. Following both sets of cases, comparisons are drawn between the statistical and semi-deterministic methodologies. Finally, some problems encountered in the simulation implementations, including Doppler filter design and sampling-rate conversion, are discussed.

5.1 Simulation System

In this section, a typical simulation block diagram in simulink is demonstrated first. Following that, the simulation parameters for BT and Wi-Fi systems, as well as the noise variance calculation, are discussed.

5.1.1 Simulation Block Diagram (Simulink)

Fig. 5.1 is a typical simulation block diagram in Simulink, which represents a Wi-Fi link with Bluetooth interference in a multipath fading channel. The system mainly consists of a Wi-Fi TX/RX pair, a BT TX, and the propagation blocks. There are two different fading channel blocks for the Wi-Fi TX and Bluetooth TX. The block denoted as “dB Gain” is used to control the power level of the Bluetooth interferer, while the buffer block followed is used to adjust the different sampling rates between Wi-Fi and BT transmitted signals. Finally the received signal, as the sum of these two transmitted signals, is fed into the Wi-Fi RX.

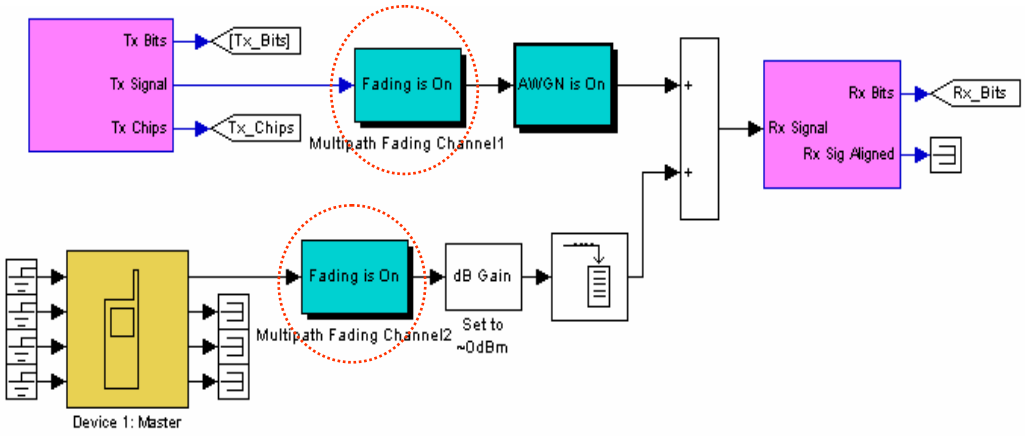

Fig. 5.1 Simulation block diagram (Simulink).

As mentioned in the beginning, we have developed the different simulation systems in Simulink to compare the BER performance by using different propagation models. In section 5.2, the results for AWGN, statistical and site-specific propagation models are demonstrated. In the statistical case, one-path and two-path channel modeling are adopted; for the site-specific case, the Wireless InSite program is used as front-end software to obtain a more accurate power-delay profile for the actual physical environment.

5.1.2 Noise Variance Calculation

In the BER vs. SNR performance simulations, it is important to obtain an accurate noise variance, according to the SNR and the system sampling rate f_s. For an unsampled system, SNR = E_b / N_o= $E_b /(2\sigma^2)$. For a given SNR, if E_b (the energy per bit) is fixed, the term $\sigma^2 = 2E_b / SNR$. When the system is sampled at f_s, the sampled noise variance can be determined by $\sigma_s^2 = f_s \cdot \sigma^2 = f_s \cdot 2E_b / SNR$. In a Bluetooth link simulation, we upsample the transmitted signal at 88 samples/bit, which results in a noise variance equal to $88 \cdot 2 / SNR$, where E_b is a unit energy per bit.

In the Wi-Fi system, which utilizes spread-spectrum technology, the processing gain needs to be considered in the calculation of the noise variance. As in upsampling, the

spreading process will also increase the simulation noise variance, which is determined by $PG \cdot 2 / SNR$, where PG is the processing gain defined by the chip rate divided by the bit rate in the spread-spectrum modulation used.

5.1.3 Parameters for Link Simulation

The system parameters for Bluetooth and Wi-Fi links are listed in Table 5.1 and Table 5.2, respectively. It is important to note that when Wi-Fi transmits at 11 Mbps, both BT and Wi-Fi systems have the same channel sample time; thus these two systems can be summed directly for the interference study. For simplicity, only the 11-Mbps Wi-Fi data rate is tested in our simulation for Wi-Fi links. The BT links are assumed to use the pure-data (DM) format.

5.2 Simulation Results

In this section, a variety of propagation cases are examined based on protocols, channel characteristics and power levels as well as interfering devices. For the Wi-Fi physical layer performance, we provide the BER results for pure AWGN, a Rician channel, and in the case of protocol coexistence, the cross-interference cases for both Wi-Fi and Bluetooth. A corresponding procedure is applied for Bluetooth systems. In the following, the BER performance for the AWGN-only case is presented, followed by one-path and two-path fading channels and finally extended to the more realistic propagation channel model obtained from the Remcom Wireless InSite front-end field calculator.

5.2.1 AWGN Case

The classic AWGN-only channel model provides a useful benchmark for the undergoing BER performance measurement through software simulation, although it represents an idealized environment, which in practice (except in deep-space applications) is not achievable. However, the biggest advantage of studying the AWGN channel is to provide accurate analytic expressions of the BERs for different modulation schemes which can be set as asymptotic estimates for performance in practical environments.

Table 5.1 Bluetooth link simulation parameters.

Data Type	Frame period (sec)	Frame size (sample)	Channel sample time (sec)
DM[1]	0.000625	55000	1.1364×10^{-8}
HV1[2]	0.000625	55000	1.1364×10^{-8}
HV2	0.000625	55000	1.1364×10^{-8}
HV3	0.000625	55000	1.1364×10^{-8}

Table 5.2 Wi-Fi link simulation parameters.

Bit Rate (Mbps)	Frame period (sec)	Frame size (sample)	Channel sample time (sec)
1	0.001048 x 8	92224	1.1364×10^{-8}
2	0.000536 x 8	47168	1.1364×10^{-8}
5.5	0.00021018 x 2	18496	1.1364×10^{-8}
11	0.00011709	10304	1.1364×10^{-8}

[1] DM: Data-Medium Rate.

[2] HV: High quality Voice.

5.2.1.1 Wi-Fi (IEEE 802.11b)

The Wi-Fi BER is plotted in Fig. 5.2 for an AWGN channel and three coexistence interference cases, in which Wi-Fi systems are both the desired and interfering devices with signal-to-interference ratios (SIRs) of 0 dB, 6 dB, and 10 dB, respectively. Observe that when the two Wi-Fi devices have equal powers, the desired device is almost shut down and cannot function at all. When the interference power is 10 dB down from the desired signal power, the Wi-Fi can operate quite well. Note that the Wi-Fi interferer(s) are assumed to operate in the same bandwidth as the desired one. If not specially mentioned, all the following Wi-Fi cases follow this assumption.

In the case of a Bluetooth device as the interferer, the Wi-Fi system BER performance is shown in Fig. 5.3, which the same conditions mentioned above are applied. Comparing the curves with Fig. 5.2, the Bluetooth interferer results in less performance loss than the Wi-Fi interferer does. This can be expected from the theoretical point of view, since the Bluetooth uses frequency hopping with a 1-MHz channel separation, while the Wi-Fi interferer is presumed to operate in the same band as the desired device. The effective rejection factor is nominally 22, or about 12 dB, which is the bandwidth ratio of the Bluetooth interfere to the Wi-Fi receiver; in terms of the spread-spectrum process gain, it varies from about 8 to 13 dB, based on the Wi-Fi bit rate. Actual interference levels with real systems will be somewhat less, since Bluetooth generally occupies one of 79 possible 1-MHz channels and does not always stay within the Wi-Fi bandpass, as assumed here Thus, these curves represent peak BER values; the long-term average will be less by rough the factor of 10 dB.

5.2.1.2 Bluetooth

Fig. 5.4 shows the Bluetooth BER performance for an AWGN channel, which is denoted by the dotted line; the other three solid marked lines present the BER results in the different SIR cases of 0 dB, 6 dB, and 10 dB, respectively. It is also assumed that the interfering Bluetooth device is always co-channel with the desired system; i.e. has exactly the same hopping sequence. It can thus be concluded that with equal-power interference

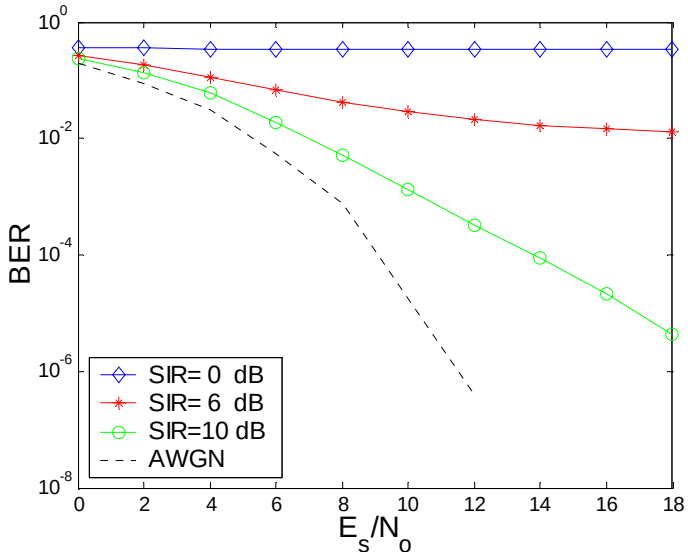

Fig. 5.2 Wi-Fi link with Wi-Fi interference in an AWGN channel.

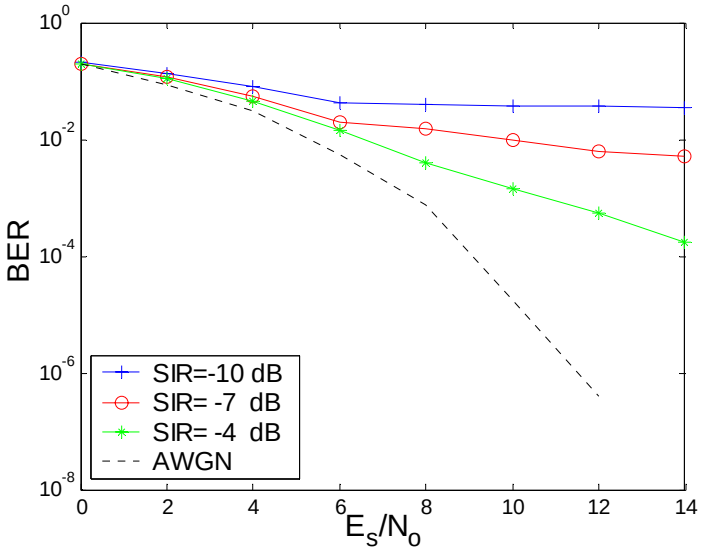

Fig. 5.3 Wi-Fi link with BT interference in an AWGN channel.

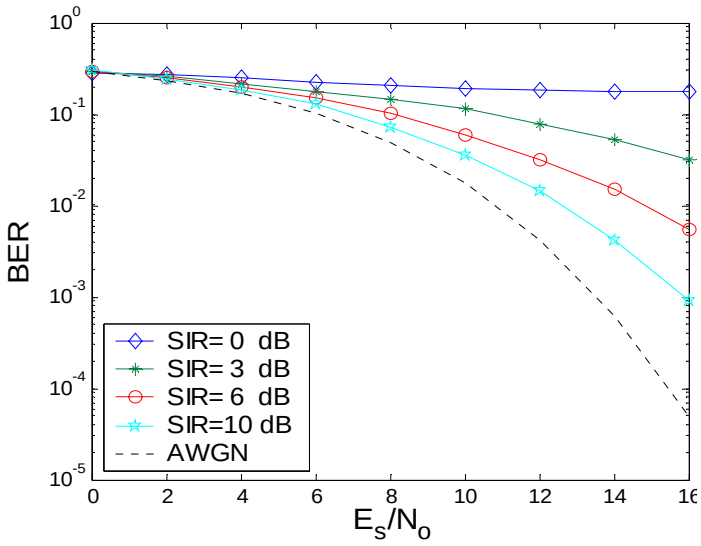

Fig. 5.4 BT link with BT interference in an AWGN channel.

from a Bluetooth device (SIR=0 dB), the desired Bluetooth receiver cannot acquire the information at all; with an SIR of 6 dB, it can work fairly well, and at an SIR of 10 dB or higher, its performance is adequate.

Fig. 5.5 shows the Bluetooth BER performance with a Wi-Fi interferer in an AWGN channel, as well as four solid-marked lines representing the BER results in the different SIR cases of 0 dB, 10 dB, 15 dB, and 20 dB, respectively. Since the Wi-Fi signal has a 22-MHz bandwidth, its interference to the Bluetooth receiver is reduced by (1) the 1-MHz Bluetooth input bandwidth, and (2) the Bluetooth hopping, which does not alter the peak BER but will lower the long-term average BER by the (22/79) bandwidth ratio.

5.2.2 Rician Fading

In the section, BER performance plots Wi-Fi and Bluetooth systems for one-path Rician channels are presented. In the one-path channel model shown in Fig. 5.6, we assume that the path consists of two components: the deterministic (specular) part and the diffused part. Following the BER curves in terms of the different given Rician factors K, where K is the ratio of the specular (direct) path power to the scattered power (see Chapter 3).

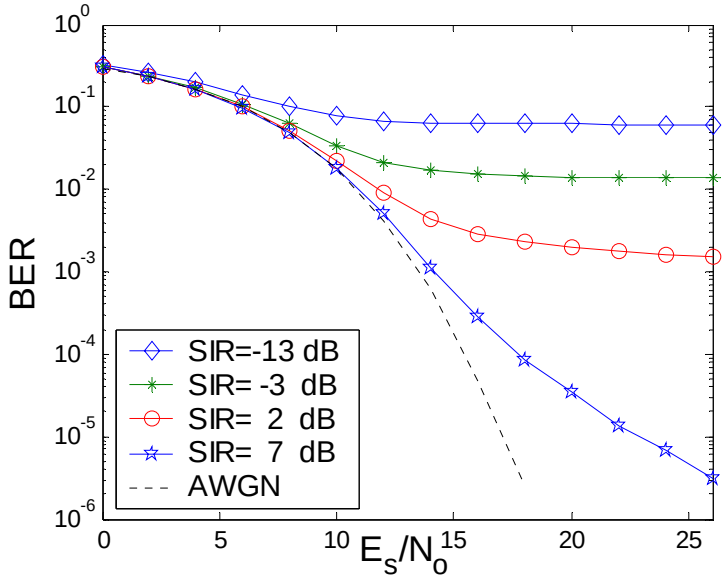

Fig. 5.5 BT link with Wi-Fi interference in an AWGN channel.

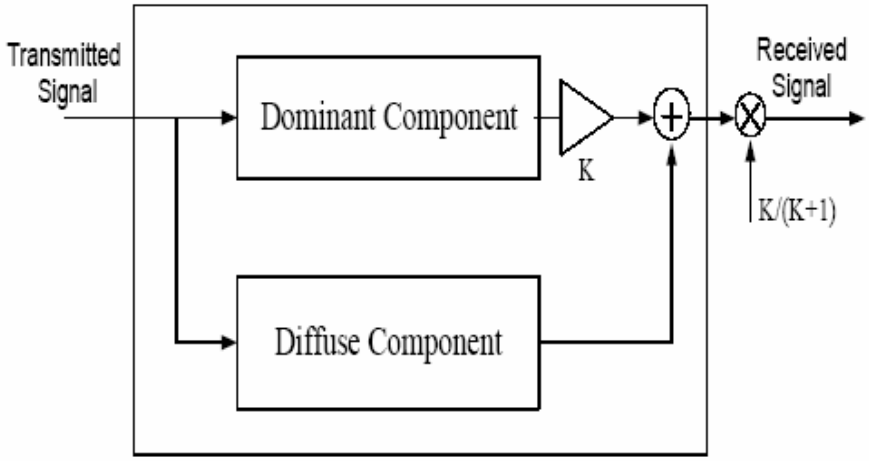

Fig. 5.6 One-path channel model.

5.2.2.1 Wi-Fi

In the following, three different types of Wi-Fi link performance are presented, which are: (1) without interference, (2) with Wi-Fi interference, and (3) with Bluetooth interference.

Fig. 5.7 shows the BER performance in a Rician channel with Rician factor K of 0, 4 and 10 respectively. The BER curves approach AWGN performance as K increases, which can be easily understood in that the more specular signal is received compared with scattered power, the "cleaner" the channel appears.

Fig. 5.8 and Fig. 5.9 show Wi-Fi link performance in a Rician fading channel with Wi-Fi interference and Bluetooth interference respectively. Comparing these two plots, it can be concluded that the Wi-Fi device with a Wi-Fi interferer will function worse than the one with a Bluetooth interferer, since the required SIR in BT interference is much less than in Wi-Fi interference to achieve the same error rate. As mentioned previously, the main reason is that the despreading process in the Wi-Fi receiver can decrease the interference level from BT by 10 dB.

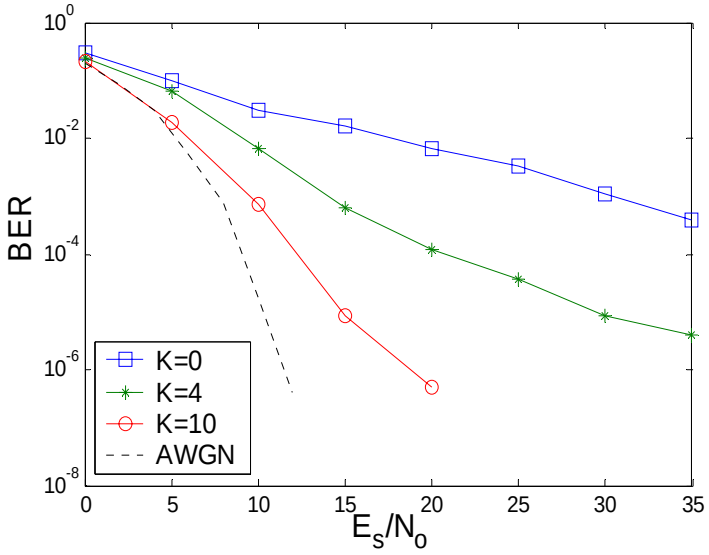

Fig. 5.7 Wi-Fi device performance in a Rician fading channel.

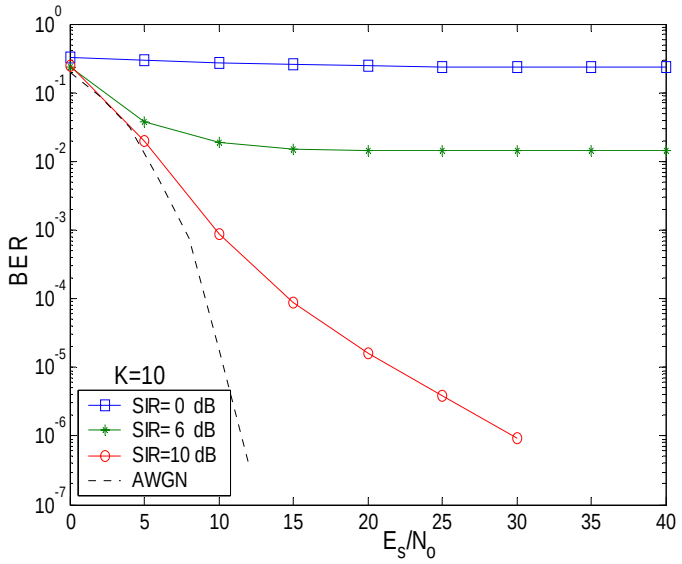

Fig. 5.8 Wi-Fi Link with Wi-Fi interference in a Rician fading channel.

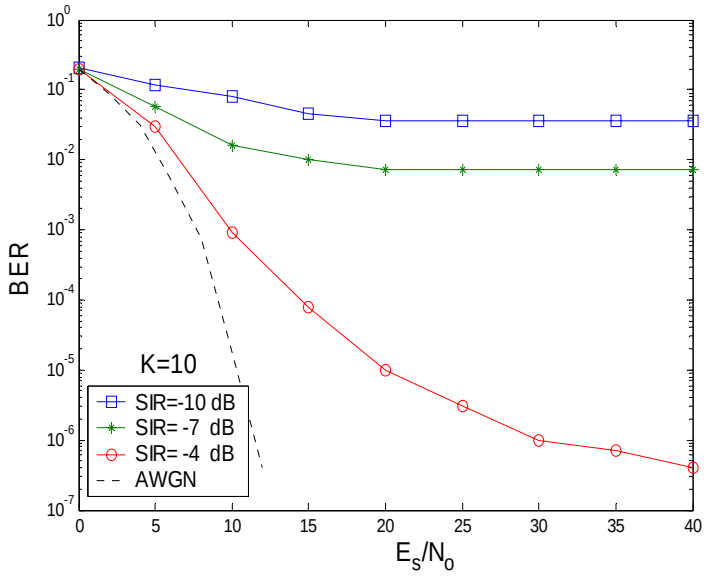

Fig. 5.9 Wi-Fi Link with BT interference in a Rician fading channel.

5.2.2.2 Bluetooth

Fig. 5.10 depicts the BER performance of a Bluetooth system in a Rician fading channel, in terms of the Rician factor K. As can be seen in the above, the BER decreases with increasing Rician factor K. Observe the waterfall curves: in the case of K equal to 0, which represents pure Rayleigh fading, the system exhibits the worst performance; when K is equal to 4 and 10, the BERs approach the error floor at SNRs of approximately 30 dB and 40 dB, respectively. When K is increased to 20, the BER curve decreases most rapidly and the trend to asymptotically approach an error floor is not observed when the SNR is less than 45 dB.

There are three sets of BER curves of Bluetooth links with Bluetooth inference shown in the Fig. 5.11(a), with different SIRs of 0 dB, 6 dB and 10 dB respectively. For each specific SIR case, two BER curves are presented in terms of Rician factors of 4 and 6. As can be seen in the plot, the performance of K = 6 is better than that of K = 4, and the performance in these two types of cases is increased as the SIR increases. The same system scenario with an SIR of 10 dB is simulated using four different K values: 6, 10, 15 and 20. The corresponding results are presented closer in Fig. 5.11(b). Obviously, when K increases, the BER performance becomes progressively closer to that of a pure AWGN channel.

When an interferer is a Wi-Fi device instead of Bluetooth, the BER performance in terms of SIR and Rician factors is obtained in Fig. 5.12 (a) and (b). From Fig. 5.12 (a), it can be concluded that the error floors of the BER curves are determined by the parameter of SIR. When SIR is equal to 20 dB, the Bluetooth link has a performance close to that of an AWGN case. In Fig. 5.12 (b), the different K values of 0, 6 and 10 are adopted for the same system, with an SIR of 10 dB. All these three curves fall in a similar manner toward their error floors, which verifies the previous conclusion.

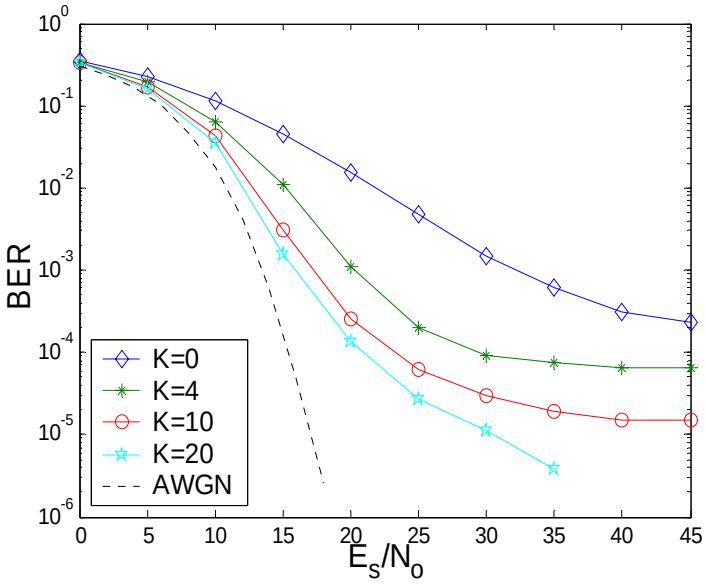

Fig. 5.10 BT link performance in a Rician fading channel.

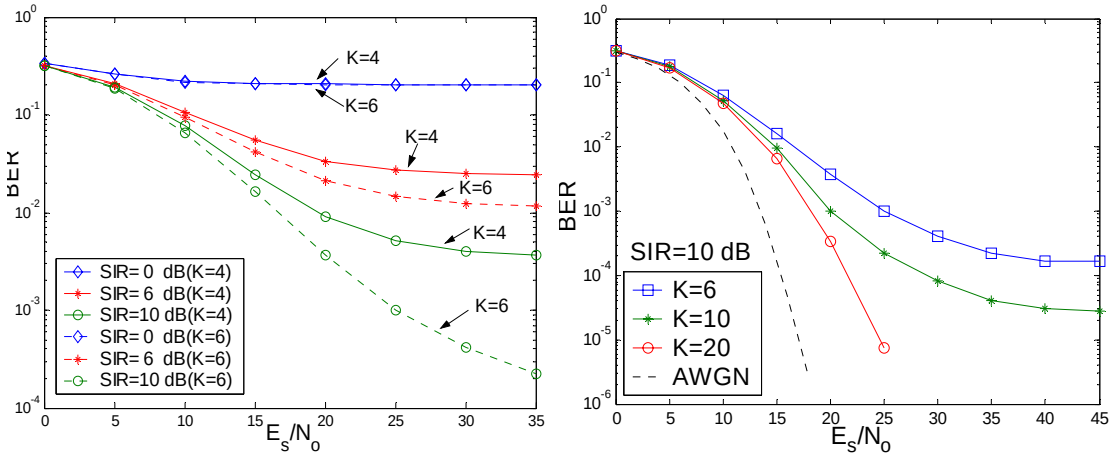

(a) (b)

Fig. 5.11 BT Link with BT interference for (a) different values of K and SIR, (b) different values of K with fixed SIR, in a Rician fading channel.

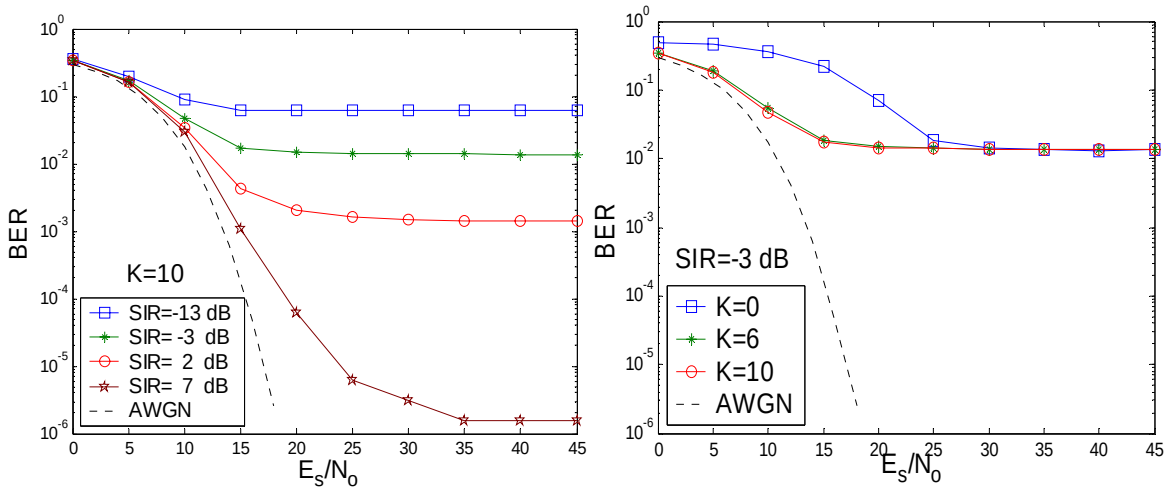

(a) (b)

Fig. 5.12 BT Link with Wi-Fi interference for (a) different values of SIR with fixed K, (b) the different values of K with fixed SIR, in a Rician fading channel.

5.2.3 Rician Path with Secondary Rayleigh Distributed Path

In the following, the frequency-selective channel models are simulated. Similar scenarios are adopted except for the propagation model itself. In the two-path channel model, shown in Fig. 5.13, there are several propagation parameters to be considered, including path gain, delay, and statistical distribution (Rician or Rayleigh) with different Rician factor and so on.

5.2.3.1 Wi-Fi

Fig. 5.14 (a) shows the results for Wi-Fi-only system in a two-path channel model with the delay between these two paths of one sample time in the system simulation, which is approximately 11.364 ns. In the case of the second-path gain of 10 dB down from the direct path, the link performance increases with increasing K. Compared with the one-path case given by Fig. 5.7, the corresponding BER increases, in that the second Rayleigh-distributed path introduces additional impairment to the whole system. When K is fixed at 10, the performance corresponding to the two different gain values of 0 dB

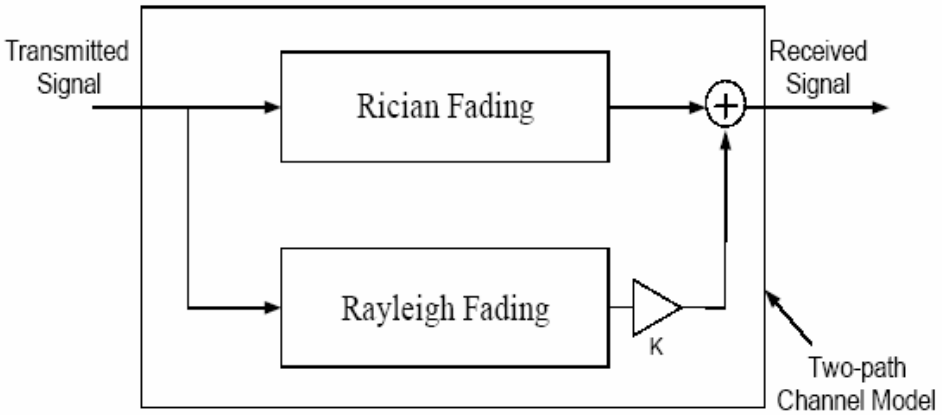

Fig. 5.13 Two-path channel model.

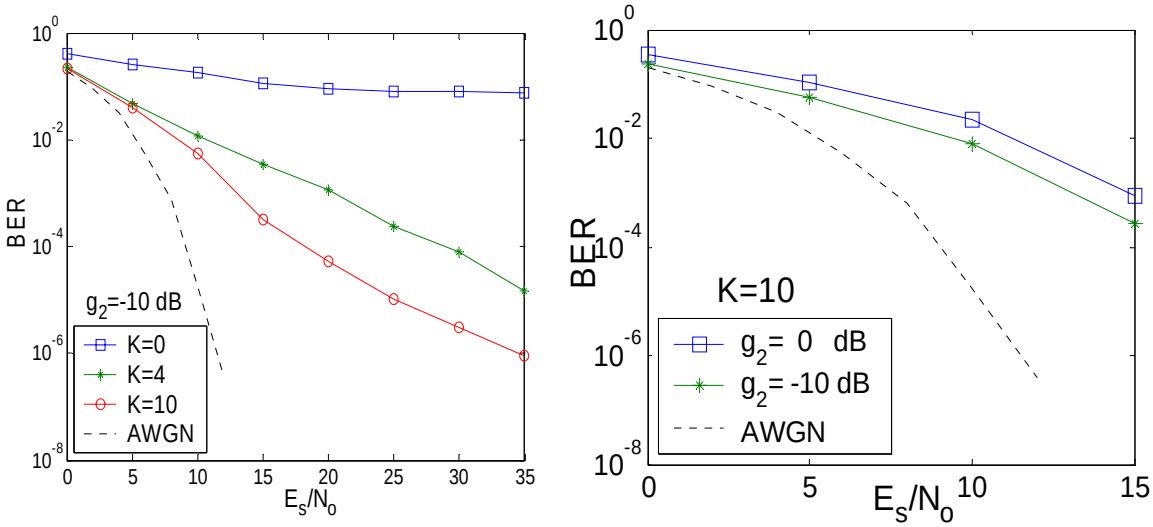

(a) (b)

Fig. 5.14 Wi-Fi only link performance for (a) different values of K, (b) different values of g_2 in a two-path channel.

and 10 dB down from the direct (first) path is presented in Fig. 5.14 (b). The case with the lower gain in the second path has better performance, which is consistent with our expectation.

When there are two Wi-Fi transmitters present in the system, the link performance becomes worse in terms of the power level of the interference Fig. 5.15 shows the BER results with different SIR values for the case of K equal to 4 and the power of the second-path 10 dB down from that of the direct path.

Fig. 5.16 presents the BER performance for Wi-Fi link with a Bluetooth interferer. As can be seen in the figure, then BERs are improved with the increasing SIR values. However, an error floor still occurs since the secondary path is pure Rayleigh fading, andthus becomes the limiting link performance factor.

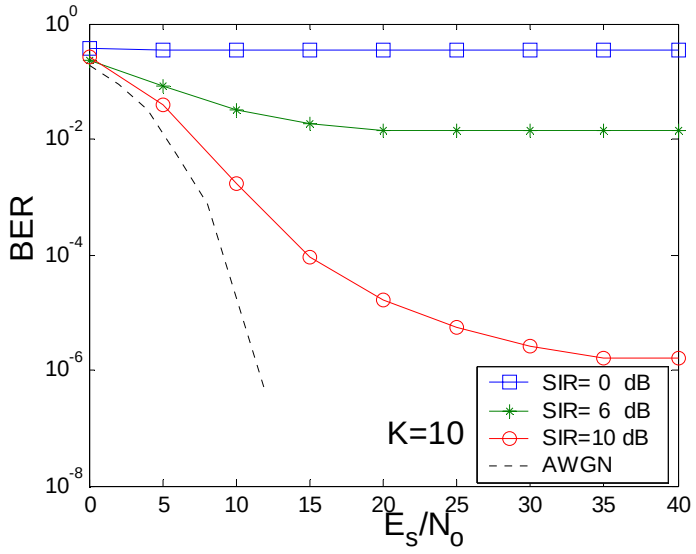

Fig. 5.15 Wi-Fi link with Wi-Fi interference in a two-path channel (K=10, g_2 =-10 dB).

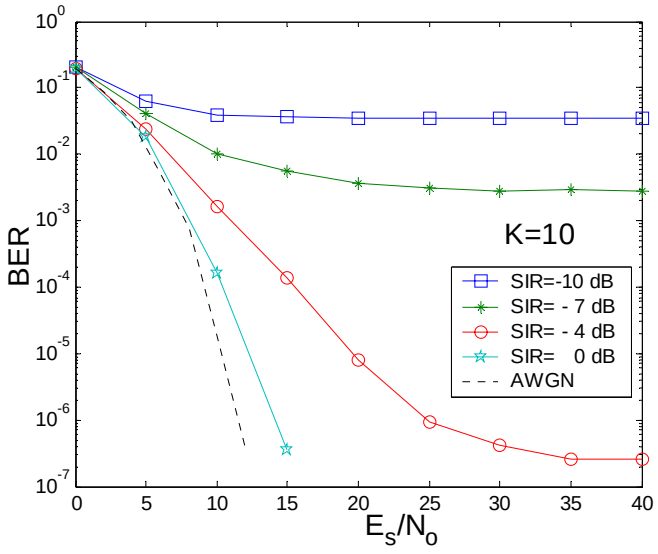

Fig. 5.16 Wi-Fi Link with BT interference in a two-path channel (K=10, g_2 =-10 dB).

5.2.3.2 Bluetooth

First, the Bluetooth link system without interference is simulated and the corresponding results are presented in Fig. 5.17. In the simulation, two sets of BER curves are obtained according to K values of 10 and 20. For each K value, the BER performance is improved by decreasing the secondary path gain, denoted by g_2, which is normalized to that of the direct path. Different path delays also have an influence on the BER performance. The following figure result from the modeling of different delays for the second path.

Fig. 5.18 presents the results for Bluetooth link performance with Bluetooth interference in the case of a second-path gain of 20 dB down from the direct path and its delay of 1/8 symbol period and a first-path Rician factor of 6. As can be seen in the plot, the BERs are improved as the SIR increases; when the SIR reaches 10 dB, the system functions fairly well.

Fig. 5.19 depicts the BER performance for the Bluetooth link with Wi-Fi interference. In the simulation, the Rician factor K of first path is assigned as 10, while the secondary

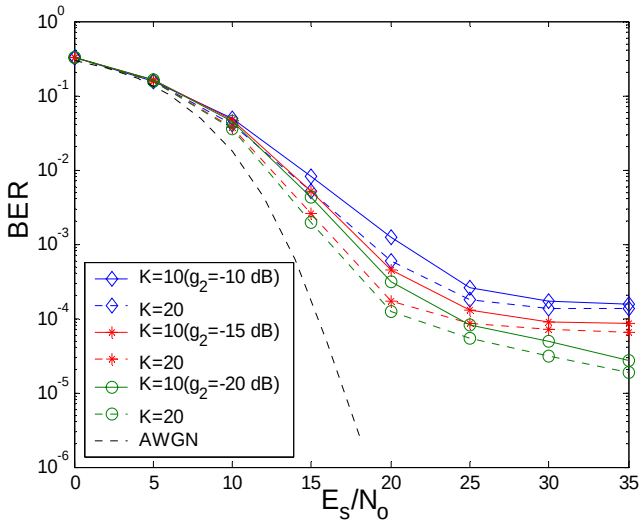

Fig. 5.17 BT link in a two-path channel.

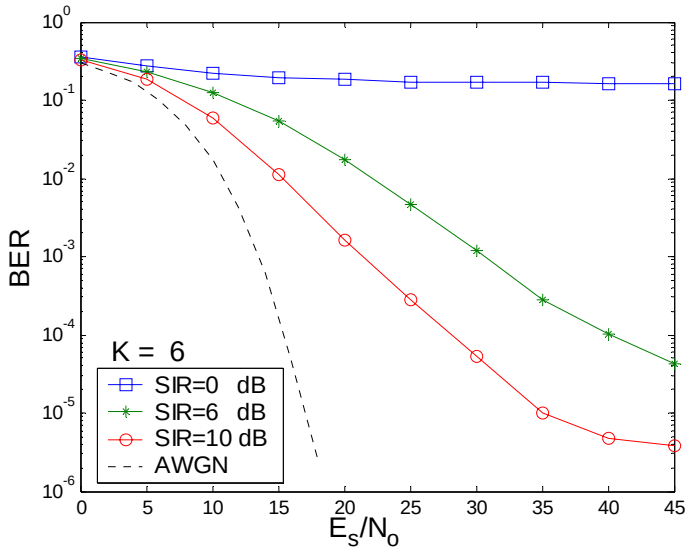

Fig. 5.18 BT link with BT interference in a two-path channel (g_2=-20, τ_2= 1/8 symbol period).

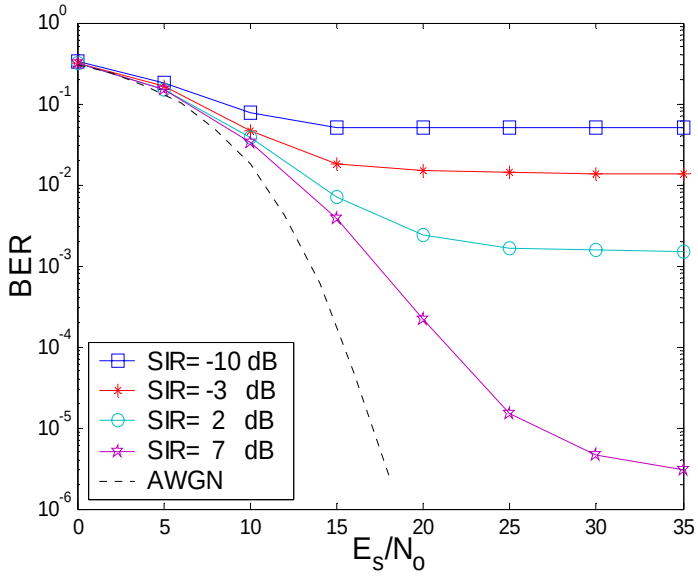

Fig. 5.19 BT link with Wi-Fi interference in a two-path channel (g_2=-20, τ_2= 1/8 symbol period).

path gain is 10 dB down and its delay is 1/8 symbol period. As shown in the plot, the BER performance is adequate when the SIR is equal to 20 dB.

5.1.4 Site-Specific Case

In this section, the more physically realistic propagation models introduced by the Remcom InSite software are applied in the calculation of BER performance. There are two types of environments adopted: one is a concrete-wall case, and the other is a metal-wall environment. As in the previous discussion, the BER results of these three system setups for both Wi-Fi and Bluetooth links are presented.

5.1.4.1 Wi-Fi

Fig. 5.20 shows a Wi-Fi link without interference for both metal and concrete-wall cases. The simulation results with K of 0, 4 and 10 are given in this plot, where these two cases are denoted by solid and dotted lines respectively. The results are consistent with the

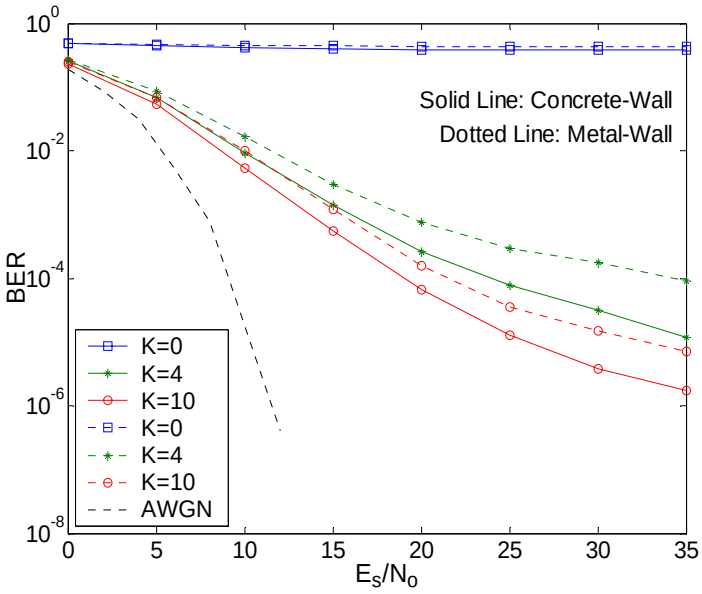

Fig. 5.20 Wi-Fi link with concrete and metal wall environments.

theoretical expectation that the metal-wall introduces more reflections and correspondingly less transmission loss. Fig. 5.21 depicts a Wi-Fi link performance with Wi-Fi interference in both cases with a Rician factor K of 10. As can be seen in the plot, the system performs poorly with the metal environment even when the SIR is as high as 30 dB.

The comparison of Wi-Fi link performance with BT interference between concrete and metal wall environments is shown Fig. 5.22. Similarly to Fig. 5.21, the performance in concrete wall environment is better than that in metal wall environment. Here, the SIR values also drop 10 dB because of processing gain of the Wi-Fi systems. From the BER curves, it can be concluded that when a BT interferer has the same power level as the desired Wi-Fi device, the system can perform fairly well. When the interference power increases, the Wi-Fi system performance is unacceptable.

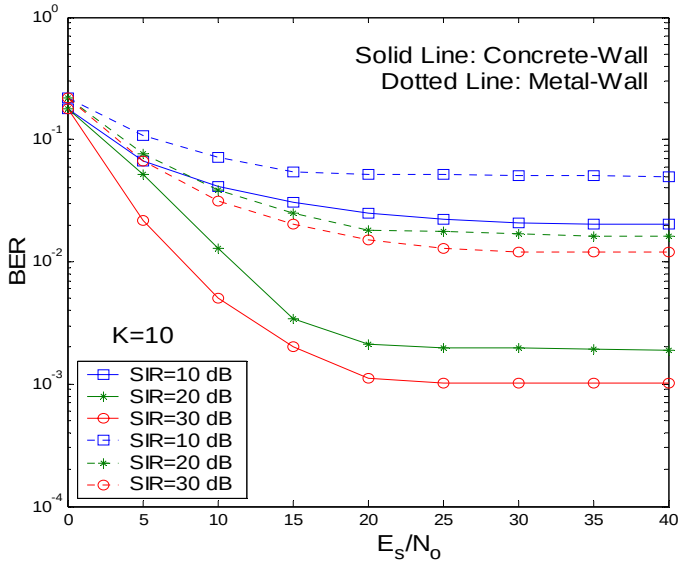

Fig. 5.21 Wi-Fi link with Wi-Fi interference in concrete and metal wall environments.

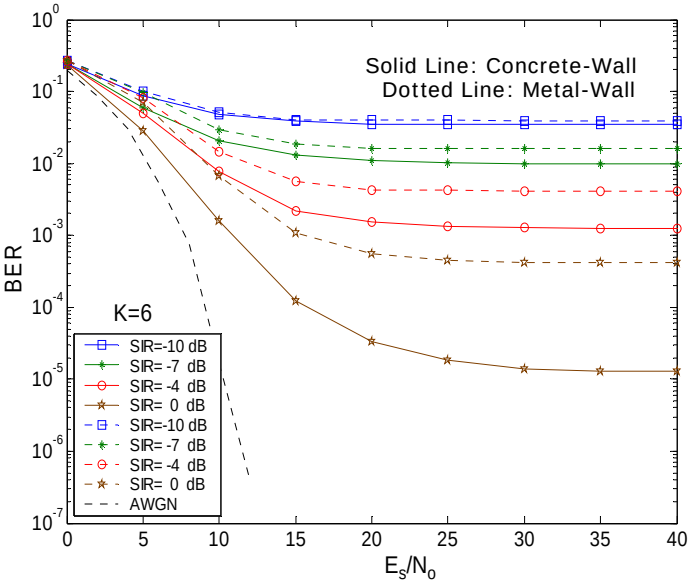

Fig. 5.22 Wi-Fi link with BT interference in concrete and metal wall environments.

5.1.4.2 Bluetooth

For the case of a Bluetooth link without any interference, the series of BER curves in terms of different values of K are given in Fig. 5.23 for both concrete- and metal-wall cases, which are presented by the solid and dotted lines respectively. Even when the path K is equal to 20, the error floor still occurs only when the SNR is approximately 30 dB. Therefore, we can conclude that the Bluetooth device does not function very well in a reflection-rich environment even the main path has a strong specular component.

The Bluetooth link performance with Bluetooth interference is given in Fig. 5.24. Three different SIR values are applied in the system simulation, and the corresponding results show that even with an SIR of 30 dB, the error floor will be achieved only when the link SNR is approximately 35 dB. Two sets of BER curves are presented for K values of 10 and 20, which are denoted by solid lines and dotted lines respectively. For each case, the SIR value is set as 10 dB, 20 dB and 30 dB. As can be seen in the plot, the performance is progressively improved when K increases, though the improvement room is smaller for the higher SIRs. Fig. 5.25 presents the BER performance with SIR of -3 dB, 2 dB, and 7 dB instead of 10 dB, 15 dB and 20 dB in the case of K=10. Comparing the two groups of curves, the performance is similar, but there is still impairment in the second case due to the deep reflections in the metal-wall environment. As mentioned before, the SIRs have 13 dB dropped because of the front-end 1-MHz bandwidth filter in the BT receiver, which filters out most of the 22-MHz bandwidth Wi-Fi interfering signal.

5.3 Comparison Study

Fig. 5.26 is the BER plot for our proposed site-specific propagation model and the two-path statistical propagation model, which was developed previously. As can be seen in these two plots, the BER performance is closer for the cases as K increases. However, there is an apparent difference when K=0. It can be expected that when the value of K increases, the propagation channel is friendlier, and both statistical and site-specific channel models become good approximations for the realistic environment. However,

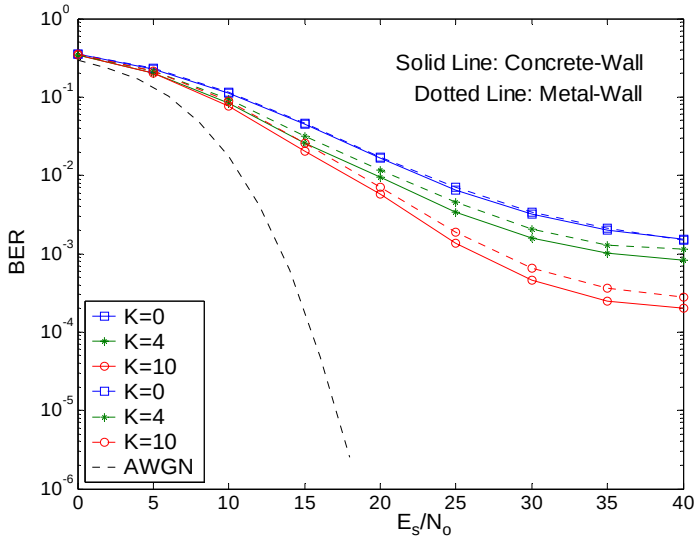

Fig. 5.23 Bluetooth only link in concrete and metal wall environments.

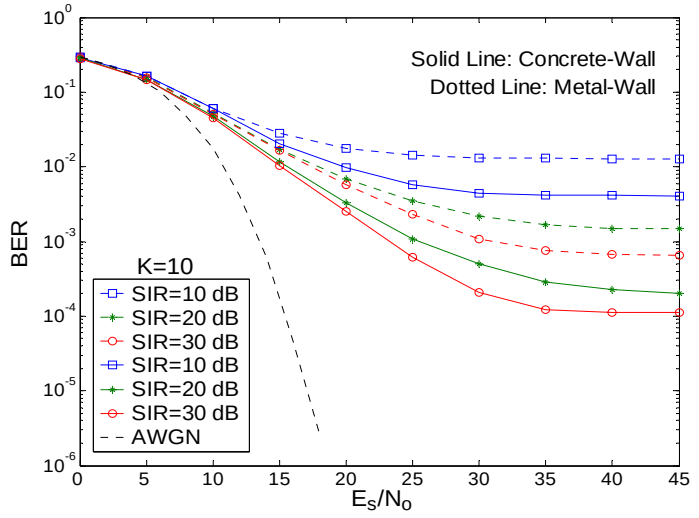

Fig. 5.24 BT link with BT interference in concrete and metal wall environments.

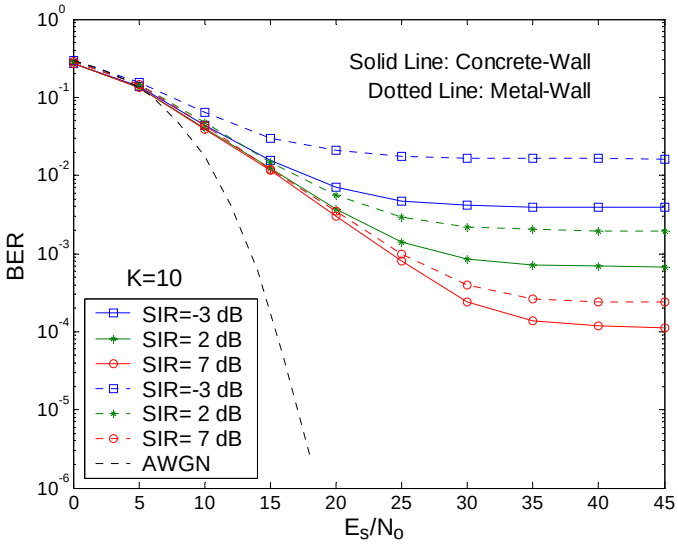

Fig. 5.25 BT link with Wi-Fi interference in concrete and metal wall environments.

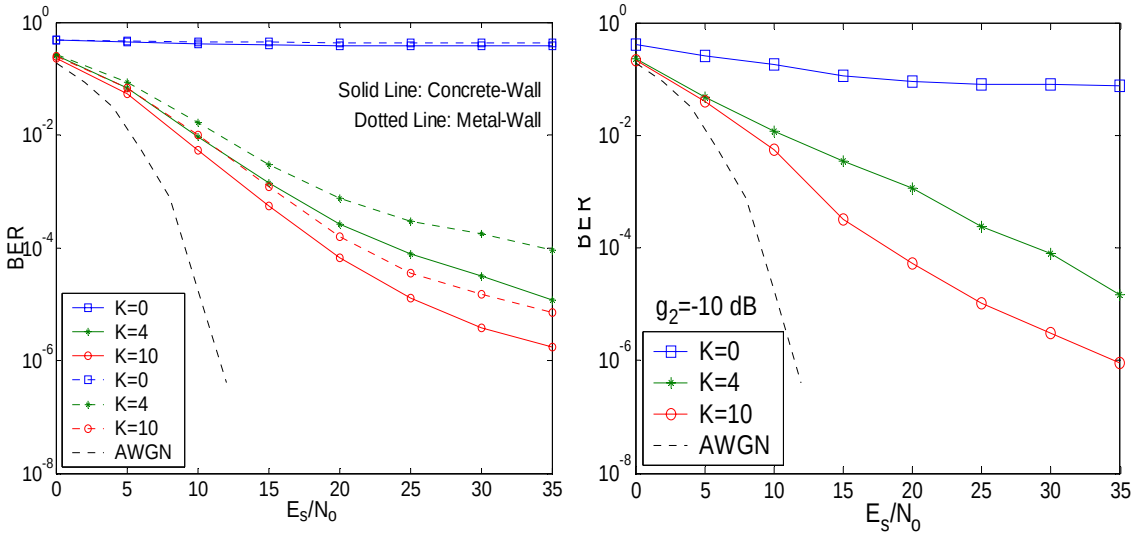

(a) (b)

Fig. 5.26 Comparison of Wi-Fi link between site-specific and two-path statistical models, (a) in concrete and metal wall environment, (b) in two-path statistical model.

when K=0, which means there is no direct component in the channel, Fig. 5.26 (b) is much different from the Fig. 5.26 (a). Thus, it can be concluded that the statistical channel has much greater approximation errors compared with site-specific model when the value of K is small. As K increases, both models are good predictors of the environment

5.4 Statistical Channel Modeling Method

5.4.1 Time Correlation - Doppler spreading spectrum

To simulate a Rayleigh fading channel, we need to generate a complex Gaussian random process with a prescribed power spectral density (PSD) or, equivalently, its autocorrelation function. In the rest of this section, two methods will be presented:

1. Time-domain method: First generate a white Gaussian process and then pass this process through a filter to obtain a colored Gaussian process. The filter must be designed to produce the desired PSD.

2. Frequency-domain method: First generate a white Gaussian process to represent the frequency components of the random process. Scale each component in order to produce the desired spectral shape. Then perform a Fourier Transform on the random sequence to produce the desired time-domain process.

Each of these methods has its advantages and disadvantages, although both are commonly used. Now, we will consider some extreme cases using the frequency-domain method. For short simulations, the number of bits may be less than the inverse of the normalized Doppler frequency (Doppler period). Obviously, this situation will lead to erroneous results for simulations of short length. For very slow fading channels, i.e., approximately constant channel parameters), we may choose one discrete frequency component to represent one step in the time-domain process. This method may be not very reliable in all cases. Moreover, the computational complexity gets high for large simulation lengths due to the FFT process used within this method. On the other hand,

the filter designing in the time domain may lead to unstable responses and require complex power spectrum estimation techniques to achieve the desired power spectrum. Thus, each method has significant difficulties.

Considering in the Simulink environment there are powerful filter design functions for the time domain, only the second method is used for our implementation of the fading random process. The procedure for generating a realization of the Rayleigh fading process in time domain is summarized below: Step 1: Given the maximum Doppler frequency f_d and system simulation sampling rate f_s, design the filter transfer function H(z). Step 2: Compute the impulse response h[n] of H(z). Denote n_0 as the point where h[n] becomes negligible. Step 3: Normalize H(z) by its gain so that the filter produces an output with unit power if input is also unit-power. Step 4: Create an input signal (zero-mean, unit-power complex Gaussian) of length n_0 and run the signal through the filter to eliminate any transients. Step 5: Generate an input sequence (zero-mean, unit-power complex Gaussian) whose length is the desired length of the simulated process. Run the input through the filter and take the output time-sequence as a realization of the fading process.

We take the following steps to develop the desired Doppler filter under the specific sampling frequency, which is 2.5×10^6 times greater than the Doppler frequency in our simulation. The starting point is to build the basic IIR Doppler filter according to a specific sampling frequency. We have used two sets of filter coefficients for implementation, one is from the MATLAB built-in Simulink block, and the other is from reference [31].

Set A

The overall numerator and denominator coefficients for the filter, denoted as a and b, are listed in Table 5.3. Correspondingly, the frequency domain response and zero-pole plane plot of this filter are shown in Fig. 5.27 and Fig. 5.28. Referring back to Fig. 3.6, the amplitude response agrees with the Jakes Doppler spectrum very well. Although the phase response is not linear, it will not have very much effect on the statistical

Table 5.3 IIR filter coefficients (Set A).

a	1.0000	7.9309	-27.5268	-54.6113	67.7362	53.7862	-26.7012	-7.5767	0.9409
b	1.0000	-7.9110	27.4676	-54.6713	68.2294	-54.6713	27.4676	-7.9110	1.0000

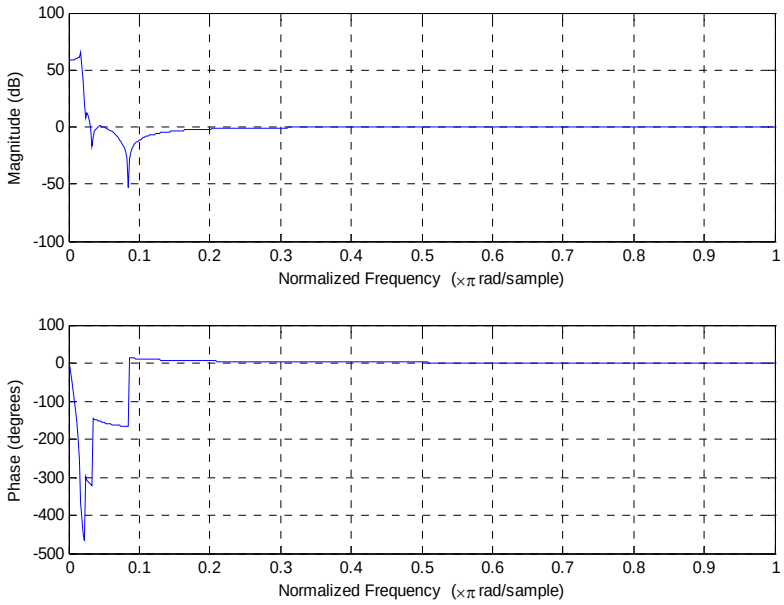

Fig. 5.27 Amplitude and phase response in the frequency domain (Set B).

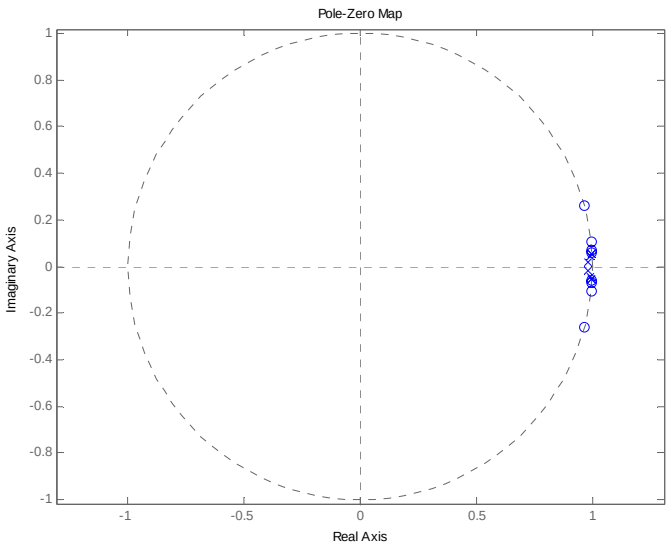

Fig. 5.28 Zero-pole plane (Set A).

characteristics of the fading simulation. Fig. 5.28 confirms that the filter is stable, since all the zeros and poles are within or on the unit circle.

Set B

Table 5.4 shows the IIR filter coefficients for Set B. Similarly to set A, the amplitude and phase response in set B can be the ideal at the same time. The normalized cutoff frequency is 0.667 instead of 0.0018 in set A. Accordingly, the frequency-domain response and zero-pole plane plot of this filter is shown in Fig. 5.29 and Fig. 5.30.

As before, the filter here can be realizable because all the zeros and poles are inside the unit circle. Here we just provide the coefficient results according the Jakes model, where the specified IIR filter is used to generate the Jakes Doppler spectrum. In order to address more general cases, common power-spectrum estimation methods are used for approximation. For instance, an auto-regressive moving average (ARMA) model is used to develop the transfer function. There are some useful existing methods to implement ARMA model, including BFGS, a kind of quasi- Newton method, which uses the joint cost function to derive the AR & MA coefficients simultaneously. Most often, the AR

Table 5.4 IIR filter coefficients (Set B).

a	1.0000	1.7429	2.3339	1.3428	0.5955
b	0.7172	2.2514	1.7050	1.5129	0.5363

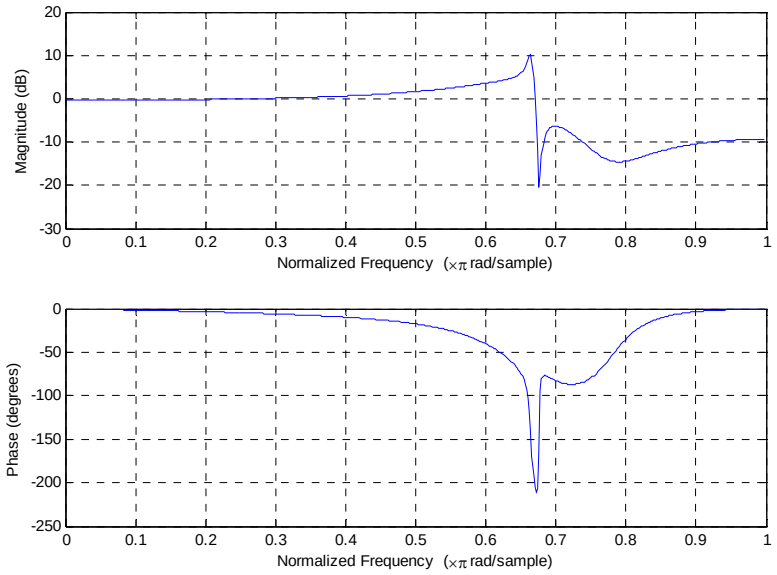

Fig. 5.29 Amplitude and phase response in the frequency domain (Set B).

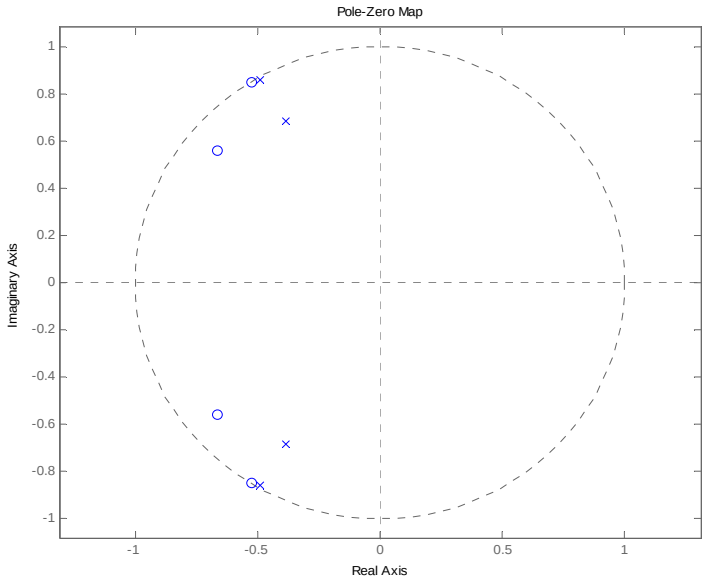

Fig. 5.30 Zero-pole plane (Set B).

coefficients are estimated first by using a Modified Yule-Walker method, and the MA coefficients are obtained by Newton-Raphson algorithm. The order of the AR & MA processes is specified by experience and not a subject of our research in this thesis.

5.4.2 Frequency Correlation (Time dispersion) – Power Delay Profile

Since the indoor wireless channel is assumed to be uncorrelated scattering wide-sense stationary (WSSUS), each path is considered independent, with the associated power and delay parameters outputted from Wireless InSite.

5.4.3 Sampling-Rate Conversion

To complete the computations for the channel model, multistage interpolation and decimation operations are utilized to produce a signal with the desired channel sampling rate, which is mathematically illustrated in Eq. (5.1),

$$\frac{I}{D} = R\left[\frac{f_{channel}}{2 \cdot f_d / f_{cutoff}}\right], \tag{5.1}$$

where I and D are the interpolation and decimation factors respectively and R[·] is the approximation function which converts the inside numerical value to the nearest rational expression. In order to reduce computational complexity while having good time-correlation accuracy, six stages of decimation or interpolation are chosen. Moreover, the interpolation rate for each stage cannot exceed 10. Here we using an FIR filter for interpolation/decimation algorithm, and the orders of the interpolation/decimation filter are estimated by a Kaiser window. For indoor cases, only the time correlations introduced by the Doppler filter are used in most research. For the case with several main reflectors in the environment, uncorrelated scatterers are assumed for simplicity, which means the correlation between any two paths is ignored. Since our application is in an industrial environment, which is between a pure indoor environment (residential or office case') and outdoor environment, the time correlations need to be considered to some degree.

There are other perspectives which need to be addressed. For instance, there is a significant tradeoff between the simulation accuracy and fading accuracy. The simulation accuracy can be improved by raising the sampling rate, but in turn this often degrades the fading accuracy, since the higher the sampling rate, the more distortion the digital filters produce. Therefore, in our work we have applied the same fading value within a given data frame in order to maintain the desired statistical characteristics for the fading channel model.

Chapter 6

Conclusions and Future Work

The principal result of this research is a validation of the new general semi-deterministic site-specific propagation modeling methodology, based on the ray-tracing field path solver incorporated into the Remcom Wireless InSite program. The InSite routines determine the specific RF path configuration followed to propagate signals from the selected transmitter location to the desired receiving spot and solve for the three orthogonal E and H field values at each interaction point (reflection, diffraction, or transmission) along each significant path. The various paths are then sorted via their respective amplitudes, retaining only the ones above a predetermined power level. The current propagation-modeling method then assigns an estimate of the statistical variation along each path, based on material properties at the interaction points, relative velocities and directions of transmitter, interaction sites, and/or receiver, and general small-scale geometry effects such as surface roughness and the like.

The basic semi-deterministic, multi-path methodology [32], [33] represents each explicit path extracted by the InSite solver program as a dithered Rician sub-channel, with individual effective path amplitude, phase, and delay parameters. The complete model adds to these the composite path polarization, which can also be obtained from the optional complex 3-D field solver built into the InSite package. We have compared these site-specific results with standard statistical models such as flat (non-frequency selective) Rayleigh and Rician fading channels and pure AWGN-only (non-fading) cases. The obvious conclusion is that the new methodology, based on the accuracy of the InSite field solver, offers a significantly higher level of accuracy in predicting RF propagation in quantifiable indoor and outdoor venues than is possible using classical statistical techniques. This advantage in turn will permit improved system deployment schemes, better understanding and assessment of diversity techniques such as multiple antennas, polarization diversity, and the use of space-time coding and/or specialized modulation schemes such as OFDM or spread-spectrum to overcome multipath effects in difficult

real-life RF environments. The extensive comparisons with the classical Rayleigh and Rician flat-fading models underscore the need for more precise RF channel models, since in some instances (e.g., strong direct-path scenarios) the statistical models yield overly pessimistic results; in other situations (such as highly or even moderately reflective environments) the flat-fading based statistical models are often far too optimistic. The other major shortcoming of most statistical propagation predictors is the assumption of totally isotropic scattering, which largely ignores the reality of strong discrete reflections and the effects of signal polarization rotations in virtually all complex RF environments. The new model presented in this work strikes a useful balance between computational requirements and prediction accuracy and permits a highly assessment of the RF signal performance in real-life indoor environments typical of large commercial and industrial spaces such as warehouses, factories, office buildings, and the like. Further, practical determinations of mutual interferences between band-sharing RF devices are essentially impossible without valid models of the respective propagation channels, due to the overwhelming effects of multipath, signal scattering, and diffraction on the integrity of the received RF signals. Due to the massive complexity of the signal formats employed in most commercial wireless protocols, we have not attempted to address all possible combinations of even the popular Bluetooth and Wi-Fi systems in such venues, but the results presented here should serve as a general indicator of general compatibility of these systems and forewarn users of potential operational difficulties in many such situations.

Future research using this semi-deterministic modeling technique should include the addition of newer protocols such as ZigBee and the OFDM forms of ultra-wideband (UWB), which are just emerging and are not yet widely available on the commercial market. In addition, other ISM-band radios, cell-phones, and popular two-way radio systems should also be addressed as time and resources permit. Circuit configurations, filtering topologies, and bit detection methods can also be effectively studied in realistic RF propagation environments to improve the performance of current and future radio hardware systems. The use of multiple antenna arrays, optimal combining, and polarization-diversity techniques are also areas to be explored by follow-on researchers in the field; the use of the model [32], [33] should prove invaluable to the development of

more advanced signal-processing techniques in the ongoing quest to boost data rates and reduce transmission errors in many types of adverse environments common to many industrial, commercial, and military applications.

List of References

List of References

[1] Wirelss Insite: “Site-specific Radio Propagation Prediction Software User’s Manual,” version 1.5.0, Remcom, Inc., State College, PA, 2003.

[2] J. McKown and R. Hamilton, “Ray tracing as a design tool for radio networks,” *IEEE Network Magazine*, pp. 27-30, Nov. 1991.

[3] T. Rappaport, *Wireless Communications, Prentice Hall*, Upper Saddle River, New Jersey, 1999.

[4] W. Stutzman, *Polarization in Electromagnetic Systems*, Artech House Boston, 1993.

[5] S. Kjesbu and T. Brunsvik, “Radiowave propagation in industrial environments,” Stanford Networking Research Center, Wireless Communications Seminar, Oct. 30, 2001.

[6] W. Jakes, ”A comparison of specific space diversity techniques for reduction for fast fading in UHF mobile radio systems,” *IEEE Transactions on Vehicular Technology*, vol. VT-20, no. 4, pp. 81-93, Nov. 1971.

[7] M. Jeruchim, P. Balaban, K. Shanmugan, *Simulation of Communication Systems: Modeling, Methodology, and Techniques*, Kluwer Academic/Plenum Publishers, New York, NY, 2000.

[8] W. Honcharenko, H. Bertoni, J. Dailing, J. Qian, and H. Yee, “Mechanisms governing UHF propagation on single floors in modern office buildings,” *IEEE Trans. on Vehicular Technology,* vol. 41, no. 4, pp. 496-504, Nov. 1992.

[9] D. Laurenson, A. Sheikh, and S. McLaughlin, “The use of ray tracing in characterising the indoor mobile radio channel,” Proceedings of the Canadian Conference on Electrical and Computer Engineering, pp. WM10.2.1-4, Sep. 1992.

[10] R. Valenzuela, “Ray tracing prediction of indoor radio propagation,” *PIMRC’94*, pp. 140-144, 1994.

[11] M. Lawton and J. McGeehan, "The application of a deterministic ray launching algorithm for the prediction of radio channel characteristics in small-cell environments," *IEEE Trans. Veh. Technol.*, vol. 43, pp. 955-969, Nov. 1994.

[12] J. Walfisch and H. Bertoni, "A theoretical model of UHF propagation in urban environments," *IEEE Transactions on Antennas and Propagation*, vol. 36, no. 12, pp. 1788-1796, Dec. 1988.

[13] W. Honcharenko, H. Bertoni, J. Dailing, J. Qian, and H. Yee. "Mechanisms governing UHF propagation on single floors in modern office buildings," *IEEE Trans. on Vehicular Technology*, vol. 41, no. 4, pp.496-504, Nov. 1992.

[14] M. Lawton and J. McGeehan, "The application of GTD and ray launching techniques to channel modeling for cordless radio systems," Proceedings 42nd VTS Conference, vol. 1, pp. 125-130, Denver, May 10-13 1992.

[15] K. Rizik, J.F. Wagen, and F. Gardiol, "Two-dimensional ray-tracing modeling for propagation prediction in microcellular environments," *IEEE Trans. Veh. Technol.*, vol. 46, pp. 508-517, 1997.

[16] P. Kreuzgruber, P. Unterberger, and R. Gahleitner, "A ray splitting model for indoor radio propagation associated with complex geometries," Proc. 43rd IEEE Vehicular Technology Conference, pp. 227-230, Secaucus, NJ, May 1993.

[17] P. Kreuzgruber, T. Bründl, W. Kuran, and R. Gahleitner, "Prediction of indoor radio propagation with the ray splitting model including edge diffraction and rough surfaces," Proceedings of the 44th IEEE Vehicular Technology Conference, pp. 878-882, June 1994.

[18] J. Wagen and K. Rizkl, "Ray tracing based prediction of impulse responses in urban microcells," Proceedings 44th IEEE Vehicular Technology Conference (VTC'94), pp. 210-214, Stockholm, Sweden, June 1994.

[19] G. Durgin, N. Patwari, and T. Rappaport, "An advanced 3D ray launching method for wireless propagation prediction," 47th IEEE International Conference on Vehicular Technology (VTC), pp. 785 – 789, May 1997.

[20] C. Yang, B. Wu, and C. Ko, "A ray-tracing method for modeling indoor wave propagation and penetration," *IEEE Trans. on Antennas and Propagation*, vol. 46, no. 6, pp. 907- 919, June 1998.

[21] Z. Ji, B. Li, H. Wang and H. Chen, and T. Sakar, "Efficient ray-tracing methods for indoor wireless communications," *IEEE Antenna Propagation Magazine*, vol. 43, no. 2, pp.41-49, 2001.

[22] K. Rizk, A. Mawira, J. Wagen, and F. Gariol, "Propagation in urban microcells with high rise buildings," IEEE VTS 46th Vehicular Tech Conf, pp. 859-863, Atlanta, GA, June 1998.

[23] G. Liang and H. Bertoni, "A new approach to 3D ray tracing for propagation prediction in cities," *IEEE Trans. on Antennas and Propagations*, vol. 46, no. 6, pp. 853-863, June 1998.

[24] S. Kim, B. Guarino, T. Willis III, V. Erceg, S. Fortune, R. Valenzuela, L. Thomas, J. Ling, and J. Moore, "Radio propagation measurements and prediction using three dimensional ray tracing in urban environments at 908 MHz and 1.9 GHz," *IEEE Trans. Veh. Technol.*, vol. 48, pp. 931-946, 1999.

[25] H. Son and N. Myung, "A deterministic ray tube method for microcellular wave propagation prediction model," *IEEE transactions on Antennas and Propagation*, vol. 47, no. 8, pp. 1344-1350, August 1999.

[26] F. Agelet et.al, "Efficient ray-tracing acceleration techniques for radio propagation modeling," *IEEE Trans. on Vehicular Technology*, vol. 49, no. 6, pp. 2089-2104, Nov. 2000.

[27] S. Fortune, "A beam-tracing algorithm for prediction of indoor radio propagation," P*roc. First ACM Workshop on Applied Computational Geometry*, pp. 76- 81, 1996.

[28] A. Rajkumar, B. Naylor, F. Feisullin, and L. Rogers, "Predicting RF coverage in large environments using ray-beam tracing and partitioning tree represented geometry," *ACM Journal of Wireless Networks*, pp.143-154, 1996.

[29] T. Funkhouser, N. Tsingos, I. Carlbom, G. Elko, M. Sondhi, and J. West, "Modeling sound reflection and diffraction in architectural environments with beam tracing," *ACM Journal of Wireless Networks*, pp.143-154, 1996.

[30] A. Bose and W. Short, "A theoretical and experimental study of noise and distortion in reception of FM signals," Massachusetts Institute of Technology, 1989.

[31] S. Fechtel, "A novel approach to modeling and efficient simulation of frequency-selective fading radio channels," *IEEE Selected Areas in Communications*, vol. 11, no. 3, April 1993.

[32] S. Smith, P. Ewing, C. Jin, and M. Howlader, "An assessment of industrial wireless protocols in the nuclear power plant environment," *To appear in Fourth American Nuclear Society International Topical Meeting on Nuclear Plant Instrumentation*, Controls and Human-Machine Interface Technologies (NPIC&HMIT 2004), Columbus, Ohio, Sep. 2004.

[33] S. Smith, P. Ewing, C. Jin, and M. Howlader, "A new site-specific propagation model for wireless communications in urban and industrial environments," *submitted to Proc. of IEEE MILCOM2004*, Monterey, CA, Oct. 2004.

Appendix

Appendix

Source code for interface between Remcom Wireless InSite and our proposed site-specific propagation model is listed as follows.

```
   function [tot_power,mean_delay,
   delay_spread,num_ref,pow_path,...
       delay_path,power1,delay1]=path_parser1(filename);
    %,doa_theta,doa_phi,aoa_theta,aoa_phi,tx,ref,rx

%%%%%%%%%%%%%%%%unit%%%%%%%%%%%%%%
%%%%
% power: dBm
% delay: sec
% length: meters
% phase: degrees(0 to 360)
% Path Loss
% Electirc Field: V/m
% Antenna Gain: dBi
%%%%%%%%
% read file
%%%%%%%%
fid=fopen(filename);
fgetl(fid);
num_rx = str2num(fgetl(fid));
%%%%%%%%
% parse the data
%%%%%%%%
if num_rx ==1
    fline=fgetl(fid);
    str=sscanf(fline,'%d');
    num_path = str(2);
    sprintf('%e',num_path);
    fline=fgetl(fid);
    str=sscanf(fline,'%e %e %e');
    tot_power = str(1);
    mean_delay = str(2);
    delay_spread = str(3);
```

```
    for i=1:num_path
        fline=fgetl(fid);
        str=sscanf(fline,'%d %d %e %e %f %f %f %f');
        num_ref(i) = str(2);
        pow_path(i) = str(3);
        delay_path(i) = str(4);
        doa_theta(i) = str(5);
        doa_phi(i) = str(6);
        aoa_theta(i) = str(7);
        aoa_phi(i) = str(8);
        fgetl(fid); fline=fgetl(fid);
        if i==1
            tx(1:3)=transpose(sscanf(fline,'%e %e %e'));
        end
        for k=1:num_ref(i)
            fline=fgetl(fid);
            ref(i,k,1:3)=transpose(sscanf(fline,'%e %e %e'));
        end
        fline=fgetl(fid);
        if i==1
            rx(1:3)=transpose(sscanf(fline,'%e %e %e'));
        end
    end
end
fclose(fid);
array=find(pow_path>(max(pow_path)-20));
power=pow_path(array); delay=delay_path(array);
%%%%%%%%%%%%
% simiplify the path sets
%%%%%%%%%%%%
power0=power;
delay0=delay;
idx=floor(delay0/1e-8);
ii=1;
for i=min(idx):1:max(idx)
    arr=find(idx==i);
    if ~isempty(arr)
        power1(ii)=10*log10(sum(10.^(power0(arr)/10)));
        delay1(ii)=i*1e-8;
        ii=ii+1;
    end
    clear arr;
end
```

Vita

Chen Jin was born on March 30, 1980 in Jingdezhen, Jiangxi, People's Republic of China. She received her Bachelor of Science degree in Electrical Engineering from Zhejiang University (Hangzhou, Zhejiang, China) in July 2001. From August 2002, she began her graduate study of Master of Science in Electrical Engineering at University of Tennessee, Knoxville. She has served as a Graduate Research Assistant in the UT Wireless Communications Research Group (WCRG) and the ORNL RF & Microwave System Group. Her research work has focused on wireless channel modeling and coexistence and interference analysis of wireless LAN protocols.